The effect of streamflow, ambient groundwater, and sediment anisotropy on hyporheic zone characteristics in alternate bars

(Article begins on next page)

19 April 2024

**Correspondence to:**
A. Monofy,
ahmed.monofy@polito.it

# The Effect of Streamflow, Ambient Groundwater, and Sediment Anisotropy on Hyporheic Zone Characteristics in Alternate Bars

**A. Monofy[1]** and **F. Boano[1]**

[1]Department of Environment, Land and Infrastructure Engineering, Politecnico di Torino, Turin, Italy

**Abstract** The hyporheic exchange is the main driver for the biogeochemical transformations of nutrients within a river bed. The current study addresses the variations in hyporheic zone (HZ) characteristics in alternate bars due to different streamflow, ambient groundwater, and sediment anisotropy. Several simulations, using a sequentially coupled surface water-groundwater model of a synthetic reach with fully developed alternate bars morphology, were performed. Two HZs exist within the streambed; a shallow zone that is more linked to surface water, and a deep one that is more influenced by the groundwater variations. Increasing streamflow, and therefore bar submergence, decreases the hyporheic flow. The residence times distribution is bimodal, which implies the existence of two HZs . This bimodality is enhanced by anisotropic sediment conditions, while it is much milder in isotropic ones. The shallow zone residence times increase when streamflow value rises, while the residence times in the deep HZ are less affected. The mean and median residence times decrease by increasing streamflow in partially submerged case, and they are larger in fully submerged case. The hyporheic flow, area, residence times, and extent decrease by increasing groundwater fluxes. The deep zone is the most affected by the groundwater fluxes. Hyporheic flow and extent values are significantly larger in isotropic conditions than in anisotropic ones. The change in residence times values is different between the deep and shallow zones. A predictive model is driven to predict the hyporheic flux, residence times, and hyporheic depths dependence on bar submergence, ambient groundwater, and sediment anisotropy.

## 1. Introduction

The hyporheic zone (HZ) is the area where surface water and groundwater interact in sediments immediately beneath and adjacent to streams, rivers, and riverine estuaries. It possesses unique chemical and biological properties stemming from the mixing between groundwater and surface water (Hester & Gooseff, 2010), and its high potential for nutrients removal and pollutant attenuation has attracted the attention of many researchers (Galloway et al., 2019). The hyporheic flow ($Q_h$) is hydrologically defined as the volume of stream water per unit of time, which flows through the subsurface domain, *and it starts and terminates at the stream after a certain period of time* (Gooseff, 2010). The hyporheic flux ($q_h$) is the corresponding flow per unit area through the streambed. It differs from groundwater flux by its exchanging back and forth across the sediment-water interface (SWI) at a relatively small scale, typically centimeters to tens of meters; however, groundwater flow travels unidirectionally over much longer distances (Boano et al., 2014).

Geomorphic features, including alternate bars, ripples, and meanders, can play a significant role in hyporheic flow characteristics (Herzog et al., 2016). A distinctive feature of alternate bars emerges from the induced 3-D patterns of hyporheic flow due to the hydraulic head variation on its morphology (Tonina & Buffington, 2007, 2009; Trauth et al., 2013). Many studies have been carried out on the HZ characteristics in the 3-D gravel bars morphology. Laboratory experiments and 3-D dimensional modeling were conducted to investigate the effect of streamflow and bar's amplitude variations on hyporheic exchange (Tonina & Buffington, 2007). Besides, the alluvium depth can constrain the HZ extent (Tonina & Buffington, 2011). A predictive model was proposed to estimate the hyporheic residence times ($T$) dependence on bar submergence, hydraulic conductivity, and the slope of a stream reach (Marzadri et al., 2010). Moreover, the undermining effect of ambient groundwater on HZ was analyzed by Trauth et al. (2013) for fully submerged bars.

Despite these many studies, the HZ characteristics in *partially submerged bars* are not fully understood. The importance of bars with low submergence lies in their common occurrence during low stream flow periods,

**Table 1**
*Summary of the Performed Simulations (Checkmarks)*

| Groundwater fluxes | Stream flows | | | | | | |
| | Isotropic conductivity | | Anisotropic conductivity | | | | |
| $q_{bot}$ | $0.5Q_{avg}$ | $Q_{bf}$ | $0.5Q_{avg}$ | $Q_{avg}$ | $2Q_{avg}$ | $3Q_{avg}$ | $Q_{bf}$ |
|---|---|---|---|---|---|---|---|
| $q_{bot} = 0$ (neutral) | ✓ | ✓ | ✓ | ✓ | ✓ | ✓ | ✓ |
| $q_{bot} = +0.5q_{h_n}$ | - | - | - | ✓ | - | - | ✓ |
| $q_{bot} = -0.5q_{h_n}$ | - | - | - | ✓ | - | - | ✓ |
| $q_{bot} = +q_{h_n}$ | - | - | ✓ | ✓ | ✓ | ✓ | ✓ |
| $q_{bot} = -q_{h_n}$ | - | - | ✓ | ✓ | ✓ | ✓ | ✓ |
| $q_{bot} = +1.5q_{h_n}$ | - | - | - | ✓ | - | - | ✓ |
| $q_{bot} = -1.5q_{h_n}$ | - | - | - | ✓ | - | - | ✓ |
| $q_{bot} = +2q_{h_n}$ | - | - | ✓ | ✓ | ✓ | ✓ | ✓ |
| $q_{bot} = -2q_{h_n}$ | - | - | ✓ | ✓ | ✓ | ✓ | ✓ |
| $q_{bot} = +3q_{h_n}$ | - | - | ✓ | ✓ | ✓ | ✓ | ✓ |
| $q_{bot} = -3q_{h_n}$ | - | - | ✓ | ✓ | ✓ | ✓ | ✓ |

and they are the most typical configuration in mountain rivers during the spawning activity of many salmonids (Tonina & Buffington, 2007). Even though the ambient groundwater has a considerable effect on HZ characteristics (Trauth et al., 2013), to our knowledge, it has been less studied for partially submerged bars. Although sediment anisotropy is very common, no study has deeply disentangled its effect on the HZ characteristics. Here, an extensive study is carried out on the HZ characteristics in gravel bars to fill the abovementioned gaps. Therefore, the main goals of this study are to (1) deeply investigate the effect of (*a*) *bar submergence* due to different streamflows, (*b*) *ambient groundwater*, and (*c*) *sediment anisotropy* on the HZ characteristics, and (2) provide *a new set of predictive equations* to account for the variations in HZ characteristics depending on these parameters.

## 2. Methodology

The current work includes 45 numerical simulations, 43 of which have different streamflow discharges ($Q_{surf}$) and groundwater fluxes ($q_{bot}$), in addition to two simulations that were performed in isotropic conditions as a reference (Table 1). These simulations help in understanding the effect of different parameters combination on the HZ characteristics. A sequentially coupled surface water-groundwater model was built to perform the intended analysis. In other words, the flow enters only from the surface domain into the subsurface one, with no feedback on the streamflow. A synthetic stream reach, whose dimensions and characteristics are the same as the Maruia River in New Zealand (reported by Van den Berg, 1995; Table 2), was used in our simulations. However, it is important to notice that this study does not aim to analyze the hyporheic exchange in the Maruia River. The river roughness coefficient was calculated with the Manning equation for wide channels due to its large width ($w$) compared to the channel depth ($d$), as $w/d \approx 64$. The median of sediment particles within the river bed ($D_{50} = 36$ mm) is typical of gravels (Julien, 2002). Additionally, the flow data exhibit a considerable difference between the average and bankfull streamflow discharge

**Table 2**
*Hydraulic and Geometric Characteristics of the Maruia River (Van den Berg, 1995) that are Used in the Present Work*

| Stream reach characteristics | |
|---|---|
| Width ($w_{bf}$) | 87.4 m |
| Depth ($d_{bf}$) | 1.36 m |
| Sediment size ($D_{50}$) | 36 mm |
| Stream reach slope ($s_0$) | 3.49 m/km |
| Average discharge ($Q_{avg}$) | 55.8 m³/s |
| Bankfull discharge ($Q_{bf}$) | 214 m³/s |
| Sinuosity ($p$) | 1.09 |
| Manning coefficient ($n$) | 0.04 |
| **Alternate bars Geometery** | |
| Wavelength ($\lambda_{ab}$) | 271.5 m |
| Amplitude ($\Delta_{ab}$) | 1.25 m |

*Note.* The dimensions of the alternate bars were calculated with the empirical equations of (Da Silva & Yalin, 2017).
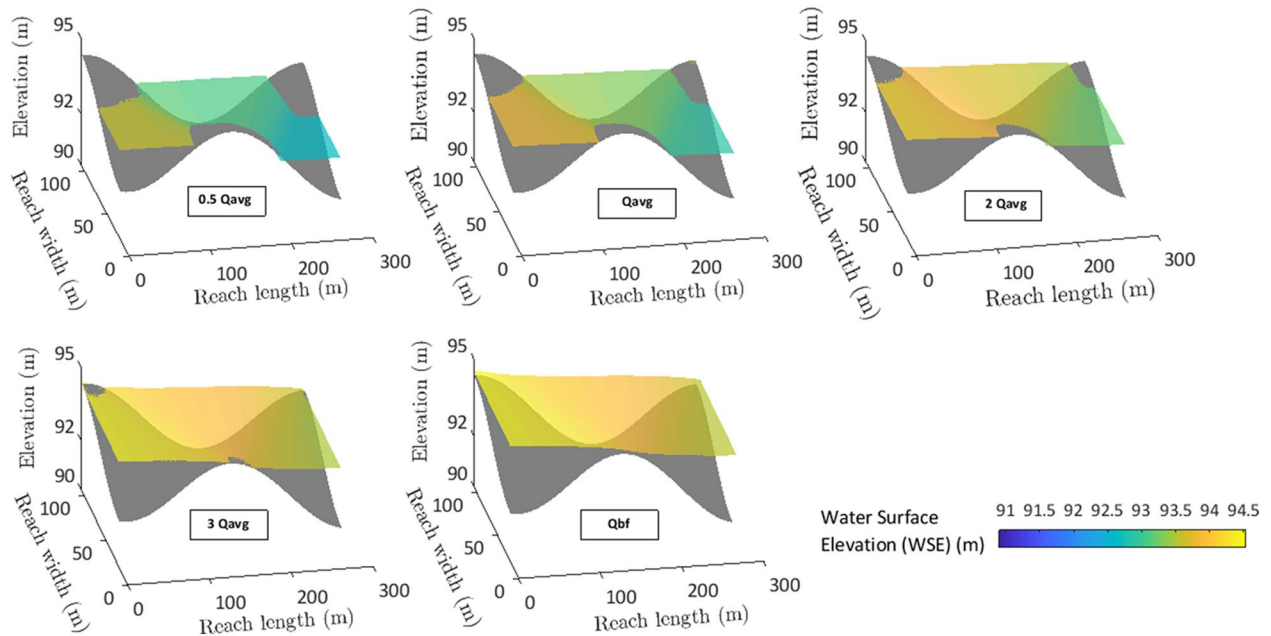
**Figure 1.** Water surface elevation for different $Q_{surf}$ cases (in black boxes) and bar submergence. The gray surface represents the streambed elevation of the middle alternate bar.

($Q_{bf} \approx 4Q_{avg}$), hence providing a sufficiently wide range to emphasize the differences in the pertinent HZ characteristics among the different submergence ratios.

### 2.1. Alternate Bar Geometry

The empirical set of equations recently developed by Da Silva and Yalin (2017) for free-formed one-row bars in wide and straight channels was used to calculate the bar dimensions (wavelength $\lambda_{ab}$, and amplitude $\Delta_{ab}$) that were imposed on the synthetic stream reach. $\lambda_{ab}$ is the distance between two successive riffle crests or pool troughs, while $\Delta_{ab}$ is half the elevation difference between a bar crest and trough. This predicting set of equations was chosen because it was derived from a worldwide data set collection of different alternate bars dimensions under bankfull streamflow conditions. The resulting bar wavelength and amplitudes were $\lambda_{ab} = 271.5$ m and $\Delta_{ab} = 1.25$ m, respectively. Subsequently, these dimensions were used to construct a gradually varying and smooth streambed using Equation 1:

$$E_{ab}\left(x, y\right) = \Delta_{ab} \sin\left(\frac{2\pi x}{\lambda_{ab}}\right)\cos\left(\frac{\pi y}{w_{bf}}\right) \tag{1}$$

where $E_{ab}$ is the streambed elevation, $x$ is the longitudinal direction (streamflow direction), $y$ is the transverse direction, and $w_{bf}$ is the reach width under bankfull streamflow. According to Equation 1, a sequence of peaks and troughs was present along each bank of the stream reach (the gray surface in Figure 1). The aspect ratio is $\frac{\lambda_{ab}}{w} \approx 3.1$, which is within the range reported in literature for free-formed alternate bars ($\approx 3-7$) (Keller, 1972; Leopold & Wolman, 1957). Therefore, this stream reach can be representative of a more common type of alternate bars.

Finally, to avoid the effect of upstream and downstream boundary conditions, a sequence of seven alternate bars was developed to define the model domain extent using Equation 1. Only the middle bar was considered for the hyporheic exchange analysis, similar to the approach followed by Trauth et al. (2013). The smoothly varying bed elevation was built using a fine spatial resolution ($\triangle x = \triangle y = 0.1$ m). Afterward, it was used as a bottom boundary for the 2D domain to calculate the water surface elevation (SWE) as well as a top boundary for the subsurface domain.

**Table 3**
*Streamflow Cases and Bar Submergence Ratios Considered in the This Work*

| Discharge ratio | Discharge value (m³/s) | Bar submergence ratio (%) | Bar submerged area (m²) |
|---|---|---|---|
| $0.5Q_{avg}$ | 27.9 | 65.74 | 18,432 |
| $Q_{avg}$ | 55.8 | 74.69 | 19,866 |
| $2Q_{avg}$ | 111.6 | 87.63 | 21,784 |
| $3Q_{avg}$ | 167.4 | 97.84 | 23,060 |
| $Q_{bf}$ | 214 | 105.16 | 23,888 |

*Note.* The bar submergence ratio associated with each streamflow case is calculated by dividing average flow depth (d) to double bar amplitude (2Δab).

### 2.2. Surface Water Modeling

A 2D model was built using the HEC-RAS 5.0.4 package to simulate different $Q_{surf}$ applied on the constructed stream reach. HEC-RAS 2D calculates SWE in $z$ direction on a defined grid mesh in a $x - y$ plane. In the synthetic stream reach, the vertical length scale is much smaller than the horizontal length scale with a smoothly varying streambed. Therefore, the hydrostatic pressure was assumed to be a good surrogate for the total hydraulic pressure at the streambed (Tonina & Buffington, 2007).

A structured grid mesh of square cells ($0.35 \times 0.35$ m²) was applied on the seven bars with a maximum cell size of 0.25 m², the minimum size of 0.09 m² and the average size of 0.12 m². The upstream and downstream boundary conditions were imposed at sections of flatbed to have a streamflow value that is uniformly distributed on the entrance and exit of the calculation domain. At the upstream boundary, five steady streamflow values ($0.5Q_{avg}$, $Q_{avg}$, $2Q_{avg}$, $3Q_{avg}$, and $Q_{bf}$ (Table 3) were imposed.

Normal depth boundary condition with the average stream reach slope value was imposed at the downstream boundary. Moreover, impermeable noneerodible bed and banks that are commonly used in such simulations (Tonina & Buffington, 2009; Trauth et al., 2013) were assumed in the surface water model. This assumption is common because the hyporheic exchange flow rate ($Q_h$) is usually ranging from 0.1% to 10% of the river flow (Thibodeaux & Boyle, 1987), and hence its influence on $Q_{surf}$ was neglected.

Hec-Ras 2D uses a time-stepping approach to solve the 2D flows even in steady-state conditions. We started with the dry bed condition with a dynamic wave and set the time step to be such that the Courant number will be below the unity in all cases. The diffusion wave equation approach was selected over the full momentum approach due to its lower computational cost (USACE, 2016). The Full momentum equations set was activated on one of the streamflow discharge cases ($Q_{bf}$), and the resulting difference in SWE between the two methods was less than 0.012 m. Therefore, the Diffusion Wave approach provided very reliable results for the surface water simulations. Finally, a 2D map of SWE was exported for each $Q_{surf}$ case to be applied afterward as a top boundary condition on the subsurface domain.

### 2.3. Groundwater Modeling

The MODFLOW Flex 2015.1 package was used to build the groundwater numerical model. MODFLOW, based on the finite-difference method, is extensively used for addressing flow problems of surface water-groundwater systems (McDonald & Harbaugh, 1988). The model domain included, in length, the prebuilt sequence of seven bars and, in-depth, five layers with a flat deep bottom ($\approx 200$ m $> 2w_{bf}$), which was designed to be deep enough to allow the hyporheic flow paths to develop vertically without any restrictions (Tonina & Buffington, 2011). At first, a finite-difference grid mesh was created under all the streamflow cases to discretize the seven alternate bars domain. The mesh was constructed with 800 cells in the longitudinal direction ($x$), 250 in the transverse direction ($y$), and five layers in-depth direction. Therefore, each cell dimensions in $x - y$ plane was 2.38 m $*0.35$ m. This cell size was chosen as it limited convergence time for all simulations; finer meshes with square cells ($0.7 \times 0.7$ m² and $0.35 \times 0.35$ m²) were tried in $Q_{bf}$ case, resulting in an error of less than 0.2% for $q_h$ compared to the chosen mesh size. Finally, in $z$ direction, the first two layers were thinner since they were used to calculate the hyporheic exchange flux (vertical Darcy flux) with Equation 2; therefore, their thicknesses were chosen to be 1 m, except for bankfull flow (0.5 m) (thinner thicknesses were tried, but model convergence was hampered). The third and fourth layers had the same depth of 50 m; finally, the deepest layer had a thickness of 100 m. The head in each cell of the first layer is the surface water hydraulic head imposed as a Dirichlet boundary condition. MODFLOW-2005 flow engine was employed to solve the subsurface water flow field in the sediment. The hyporheic exchange flux ($q_h$) was calculated using Darcy's law (Wu et al., 2018):

$$q_h = -K_v \left( \frac{\Delta H}{\Delta z} \right) \tag{2}$$

where $\triangle H$ is the head difference between the first two layers of the domain and $\triangle z$ is the elevation difference between the same layers. Homogeneous anisotropic conductivity was applied over the model domain, where the horizontal value ($K_x = K_y = K_h$) is an order of magnitude higher than the vertical conductivity ($K_z = K_v$). The first four layers were assumed to share the same characteristics of conductivity ($K_h = 10^{-3}$ m/s, $K_v = 10^{-4}$ m/s; Domenico et al., 1998), while the deepest layer was assumed to be more compacted (Nelson et al., 1994) ($K_h = 10^{-4}$ m/s, $K_v = 10^{-5}$ m/s). However, this deep and less conductive layer eventually did not affect the results of the HZ analysis, as the HZ extent is only within the first three layers (Section 3.4). Two homogeneous isotropic simulations ($K_h = K_v = 10^{-3}$ m/s for the whole domain) were added as reference cases for $Q_{avg}$ and $Q_{bf}$ to unravel the effect of the sediment anisotropy.

On the upstream and downstream boundaries as well as the domain sides, Neumann boundary conditions were applied with no-flux. On the bottom boundary, no ambient groundwater flux ($q_{bot} = 0$; neutral conditions) was assigned in the two isotropic simulations. However, for 43 anisotropic ones, a specified flux value was imposed depending on the ambient groundwater conditions (neutral, gaining, or losing).

In neutral conditions, the no-flux boundary condition was applied to the bottom boundary ($q_{bot} = 0$). Instead, positive and negative flux values to represent gaining and losing conditions, respectively, were imposed uniformly on the domain bottom (see Table 1). The values of groundwater flux ($q_{bot}$) were $\left[\pm 1, \pm 2, \pm 3\right] \times q_{h_n}$, where $q_{h_n}$ is the resulted value of $q_h$ in neutral conditions (obtained after carrying out a simulation with no-flux at the bottom layer), whereas positive and negative signs refer to gaining and losing conditions, respectively. Additionally, under $Q_{avg}$ and $Q_{bf}$ cases, four more simulation steps ($\left[\pm 0.5, \pm 1.5\right] \times q_{h_n}$) were added to have more refined results under these streamflow cases.

Then, to analyze the characteristics of the HZ, a particle tracking analysis was performed using MODPATH software with a one-day time step. As proved later by the results, this time step was able to track well the hyporheic flow paths. Particles were located with 1 m of spacing on $x - y$ plane on the middle bar. Due to the variations in the bar submerged area that corresponds to different streamflow, different particle numbers were injected into the subsurface domain (see bar submerged area in Table 3).

To only extract the hyporheic exchange flow paths, the forward particle tracking option was activated in neutral and gaining conditions to force the particles to move in the same direction of the hyporheic flux. Conversely, the backward particle tracking was employed in losing conditions. Consequently, in all cases, the hyporheic flow paths, which start and end at the streambed, were recognized and separated from the groundwater flow.

Finally, the aforementioned linked model was run to obtain the HZ characteristics under different $Q_{surf}$ and ambient groundwater conditions. The hyporheic flow paths were exported with the associated values of pressure heads at the top two layers, travel times, and depths data. The flow path flux ($q_f$), total residence times ($T$), and maximum hyporheic depths ($Z$) were assigned to each corresponding flow path. $q_f$ for each flow path was calculated by applying Equation 2 to the resulting head difference between the first two layers of the subsurface domain and assigning the resulting value to its corresponding flow path. For all the cases shown in Table 1, $q_h$ was calculated by averaging $q_f$ for all flow paths, and flux distribution maps of upwelling and downwelling fluxes with corresponding areas (later denoted as hyporheic exchange area, $A_h$) were produced. $Q_h$ ($A_h \times q_h$) is here defined as the water volume per unit time that infiltrates into the groundwater aquifer and exits back to the surface water. $T$ values of the exported flow paths were determined by the value of the last step on each path when its carried particle reenters the surface water domain. $Z$ of each flow path was calculated as the difference between the streambed elevation (the mean elevation of a flow path starting and ending points) and the elevation of the deepest point reached. The flux-weighted averaging method was used to construct residence time cumulative distribution ($T - CD$) and the maximum depths cumulative distribution ($Z - CD$) of the hyporheic flow paths.

## 2.4. Predictive Model Derivation

### 2.4.1. Data Collection

A total of 41 out of 45 simulations were used to build the regression model, as the remaining 4 (gaining and losing at $q_{bot} = 3q_h$ for streamflow discharges of $0.5Q_{avg}$ and $Q_{bf}$) were excluded because of the HZ

**Table 4**
Hyporheic Flux ($q_h$, m/s), Hyporheic Area ($A_h$) and Hyporheic Flow ($Q_h$, m³/D) in Different Streamflow Cases, and Different Values of Gaining and Losing Conditions ($q_{bot}$ is Expressed as a Fraction of the Hyporheic Flux in Neutral Condition, $q_{h_n}$).

| | $0.5Q_{avg}$ | | | $Q_{avg}$ | | | $2Q_{avg}$ | | | $3Q_{avg}$ | | | $Q_{bf}$ | | |
| | $q_h$ | $A_h$ | $Q_h$ | $q_h$ | $A_h$ | $Q_h$ | $q_h$ | $A_h$ | $Q_h$ | $q_h$ | $A_h$ | $Q_h$ | $q_h$ | $A_h$ | $Q_h$ |
| | ($10^{-7}$ m/s) | (m²) | (m³/d) | ($10^{-7}$ m/s) | (m²) | (m³/d) | ($10^{-7}$ m/s) | (m²) | (m³/d) | ($10^{-7}$ m/s) | (m²) | (m³/d) | ($10^{-7}$ m/s) | (m²) | (m³/d) |
|---|---|---|---|---|---|---|---|---|---|---|---|---|---|---|---|
| $q_{bot} = 0$ (neutral) | 5.58 | 9,070 | 437.0 | 4.71 | 9,838 | 400.2 | 3.40 | 10,892 | 319.6 | 2.76 | 11,530 | 275 | 1.78 | 11,944 | 183.8 |
| $q_{bot} = +0.5q_{h_n}$ | - | - | - | 3.49 | 7,076.2 | 213.1 | - | - | - | - | - | - | 1.55 | 8,173 | 109.8 |
| $q_{bot} = -0.5q_{h_n}$ | - | - | - | 4.26 | 6,679 | 246.0 | - | - | - | - | - | - | 1.46 | 8,319 | 105.1 |
| $q_{bot} = +q_{h_n}$ | 3.12 | 3,400 | 91.5 | 2.97 | 4,913 | 126.1 | 2.47 | 5,470 | 116.6 | 2.11 | 5,718 | 104.2 | 1.17 | 5,364 | 54.1 |
| $q_{bot} = -q_{h_n}$ | 4.59 | 3,700 | 146.6 | 3.36 | 4,584 | 133.2 | 2.34 | 6,268 | 126.7 | 1.83 | 6,269 | 99.3 | 1.16 | 5,267 | 53 |
| $q_{bot} = +1.5q_{h_n}$ | - | - | - | 2.92 | 2,370 | 59.8 | - | - | - | - | - | - | 8.07 | 3,081 | 21.5 |
| $q_{bot} = -1.5q_{h_n}$ | - | - | - | 2.97 | 3,583 | 92.0 | - | - | - | - | - | - | 8.31 | 2,959 | 21.2 |
| $q_{bot} = +2q_{h_n}$ | 2.97 | 380 | 9.8 | 3.38 | 1,053 | 30.7 | 2.83 | 1849 | 45.2 | 2.06 | 1904 | 33.8 | 6.01 | 1939 | 10.1 |
| $q_{bot} = -2q_{h_n}$ | 3.96 | 496 | 16.9 | 3.01 | 1,418 | 36.9 | 3.03 | 1766 | 46.2 | 1.68 | 1836 | 26.7 | 6.49 | 1991 | 11.2 |
| $q_{bot} = +3q_{h_n}$ | 0 | 0 | 0 | 3.44 | 237 | 7.0 | 3.22 | 467 | 13 | 2.59 | 553 | 12.4 | 0 | 0 | 0 |
| $q_{bot} = -3q_{h_n}$ | 0 | 0 | 0 | 5.03 | 272 | 11.8 | 6.06 | 280 | 14.7 | 2.45 | 394 | 8.3 | 0 | 0 | 0 |

Note. All the reported values are in anisotropic conditions.

**Table 5**

*Hyporheic Flux ($q_h$, m/s), Hyporheic Area ($A_h$) and Hyporheic Flow ($Q_h$, $m^3$/D) in Isotropic and Anisotropic Conditions, and in Neutral Condition ($q_{bot} = 0$)*

| | Isotropic condition | | | Anisotropic condition | | |
|---|---|---|---|---|---|---|
| Stream flow | $q_h$ ($10^{-7}$ m/s) | $A_h$ (m²) | $Q_h$ (m³/d) | $q_h$ ($10^{-7}$ m/s) | $A_h$ (m²) | $Q_h$ (m³/d) |
| $Q_{avg}$ | 24.9 | 9,605 | 2066.5 | 4.71 | 9,838 | 400.2 |
| $Q_{bf}$ | 11.5 | 11,256 | 1,114.6 | 1.78 | 11,944 | 183.8 |

disappearance (Tables 4, 6, and 8). The simulations were divided into two groups; a first one is in neutral conditions ($q_{bot} = 0$) containing seven simulations (corresponding to five different $Q_{surf}$; five simulations with homogeneous anisotropic, and two simulations with homogeneous isotropic conductivity), and a second one combining gaining and losing conditions ($q_{bot} \neq 0$) with 34 simulations in homogeneous anisotropic conditions.

### 2.4.2. Multiple Linear Regression

Multiple linear regression (MLR) analysis was implemented on the set of simulations, to build a set of predictive equations for $q_h$, and specific quantiles of residence times and hyporheic maximum depths ($T_{i\%}$, and $Z_{i\%}$, respectively, where $i = 10, 20, 50, 80,$ and 90). Therefore, these quantities were included in the model as dependent variables. On the other hand, the independent variables in the data group for the neutral conditions were surface water depth ($d$) and velocity ($v$), and the horizontal and vertical conductivities ($K_h$ and $K_v$, respectively). While for the gaining and losing data group, $K_h$ and $K_v$ were constant; therefore, they were removed, and the included independent variables were $d$, $v$, and $q_{bot}$.

### 2.4.3. Dimensionless Variables

Dimensionless groups of the independent variables ($d$, $v$, $K_h$, $K_v$ and $q_{bot}$) were created. For the neutral conditions, the independent variables could be used to compose two dimensionless quantities. First, the Reynolds number ($Re = \dfrac{vd}{\nu}$, where $\nu = 10^{-6}$ $m^2/s$ is the water kinematic viscosity) that represents the streamflow regime, and $\dfrac{K_v}{K_h}$ that denotes the sediment anisotropy. As in the gaining and losing conditions, simulations were performed in a single anisotropic condition, $\dfrac{K_v}{K_h}$ is constant in the combined gaining and losing data group. However, another dimensionless variable $\left( \left| \dfrac{q_{bot}}{v} \right| \right)$ was added to account for the effect of groundwater flux, in *absolute value*, on the HZ characteristics.

Three dimensionless dependent variables were also defined as $\dfrac{q_h}{v}$, $\dfrac{T_{i\%}K_v}{d}$, and $\dfrac{Z_{i\%}}{d}$. This normalization is similar to the one employed by Huang and Chui (2018) work except for $T_{i\%}$, in which $v$ is used instead of $K_v$. Using $K_v$ in the present work to normalize $T_{i\%}$ allowed for a more robust model with better fitting to the simulations results (see Section 2.4.4 for model robustness criteria) compared to using $v$.

### 2.4.4. Model Equations and Evaluation

The relationship between the dimensionless dependent and independent variables can be summarized as follows:

$$F^{neutral} = f\left( Re, \frac{K_v}{K_h} \right) \tag{3}$$

$$F^{gain/los} = f\left( Re, \left| \frac{q_{bot}}{v} \right| \right) \tag{4}$$

where $F$ represents the dimensionless dependent variables, *neutral* and *gain/los* superscripts refer to the neutral data group and the combined gaining and losing data group, respectively.

**Table 6**

*Residence Times at Different Probability Values of the Cumulative Frequency Distributions ($T_{90\%}$, $T_{80\%}$, $T_{50\%}$, $T_{20\%}$, and $T_{10\%}$; Days) in Different Streamflow Cases, and Different Values of Gaining and Losing Conditions ($q_{bot}$ is Expressed as a Fraction of the Hyporheic Exchange Flux in the Neutral Conditions, $q_{hp}$).*

| | $0.5Q_{avg}$ | | | | | | $Q_{avg}$ | | | | | | $2Q_{avg}$ | | | | | | $3Q_{avg}$ | | | | | | $Q_{bf}$ | | | | | |
| | $T_{90\%}$ | $T_{80\%}$ | $T_{50\%}$ | $T_{20\%}$ | $T_{10\%}$ | $T_{mean}$ | $T_{90\%}$ | $T_{80\%}$ | $T_{50\%}$ | $T_{20\%}$ | $T_{10\%}$ | $T_{mean}$ | $T_{90\%}$ | $T_{80\%}$ | $T_{50\%}$ | $T_{20\%}$ | $T_{10\%}$ | $T_{mean}$ | $T_{90\%}$ | $T_{80\%}$ | $T_{50\%}$ | $T_{20\%}$ | $T_{10\%}$ | $T_{mean}$ | $T_{90\%}$ | $T_{80\%}$ | $T_{50\%}$ | $T_{20\%}$ | $T_{10\%}$ | $T_{mean}$ |
|---|---|---|---|---|---|---|---|---|---|---|---|---|---|---|---|---|---|---|---|---|---|---|---|---|---|---|---|---|---|---|
| $q_{bot} = 0$ (neutral) | 98.5 | 81.5 | 36 | 4 | 3 | 64 | 97.5 | 80 | 37 | 5 | 4 | 56.5 | 95.5 | 78 | 32.5 | 8 | 6.5 | 54.7 | 95 | 76.5 | 27.5 | 10 | 6.5 | 52.3 | 94.5 | 84 | 49.5 | 14 | 10 | 59 |
| $q_{bot} = +0.5q_{hp}$ | - | - | - | - | - | - | 57.5 | 44 | 10 | 5 | 3.5 | 32.5 | - | - | - | - | - | - | - | - | - | - | - | - | 67.5 | 56 | 28.5 | 10.5 | 8.5 | 40.7 |
| $q_{bot} = -0.5q_{hp}$ | - | - | - | - | - | - | 63 | 45.5 | 8 | 4 | 3.5 | 35.7 | - | - | - | - | - | - | - | - | - | - | - | - | 68 | 57 | 30 | 11 | 9 | 41.9 |
| $q_{bot} = +q_{hp}$ | 27 | 16 | 7 | 3.5 | 2.5 | 21.7 | 41 | 27.5 | 8.5 | 4 | 3 | 28.2 | 41 | 27.5 | 10.5 | 5.5 | 3.5 | 31.5 | 38 | 23.5 | 11 | 5 | 3 | 29.6 | 47 | 37 | 15 | 9 | 7 | 29.4 |
| $q_{bot} = -q_{hp}$ | 25.5 | 11 | 4.5 | 2.5 | 2 | 18.3 | 35.5 | 15.5 | 6 | 4 | 3 | 21.2 | 45 | 29 | 11.5 | 6.5 | 4.5 | 27.6 | 40 | 26 | 13 | 7 | 4.5 | 32.7 | 49 | 39 | 15.5 | 9.5 | 7.5 | 31.9 |
| $q_{bot} = +1.5q_{hp}$ | - | - | - | - | - | - | 19 | 13 | 6.5 | 3.5 | 3 | 21.4 | - | - | - | - | - | - | - | - | - | - | - | - | 30.5 | 22 | 13.5 | 9 | 7.5 | 26.8 |
| $q_{bot} = -1.5q_{hp}$ | - | - | - | - | - | - | 22 | 14.5 | 7 | 3.5 | 2.5 | 17.1 | - | - | - | - | - | - | - | - | - | - | - | - | 31 | 22 | 13.5 | 9 | 7.5 | 15.4 |
| $q_{bot} = +2q_{hp}$ | 17 | 12.5 | 6.5 | 3 | 2 | 10.9 | 15.5 | 11.5 | 6 | 3 | 2.5 | 18 | 14.5 | 11.5 | 6.5 | 3.5 | 2.5 | 18.6 | 19 | 13 | 6 | 3 | 2.5 | 24 | 27 | 21 | 13 | 10 | 9 | 26.1 |
| $q_{bot} = -2q_{hp}$ | 9.5 | 7 | 3.5 | 2 | 1.5 | 12.2 | 13.5 | 10 | 6 | 3 | 2.5 | 17.6 | 17.5 | 14 | 8.5 | 4.5 | 3.5 | 16.3 | 21.5 | 15 | 7.5 | 4 | 1.5 | 26.8 | 26 | 20.5 | 13 | 9 | 8 | 28.4 |
| $q_{bot} = +3q_{hp}$ | 0 | 0 | 0 | 0 | 0 | 0 | 14 | 10 | 5.5 | 2.5 | 2 | 211.4 | 14.5 | 13.5 | 6 | 3 | 2.5 | 12.6 | 11.5 | 7.5 | 4 | 3 | 1.5 | 17.9 | 0 | 0 | 0 | 0 | 0 | 0 |
| $q_{bot} = -3q_{hp}$ | 0 | 0 | 0 | 0 | 0 | 0 | 10.5 | 7.5 | 4 | 2.5 | 2 | 7.3 | 14.5 | 13.5 | 6 | 3.5 | 2.5 | 11.9 | 13 | 9 | 4.5 | 1.5 | 1 | 20 | 0 | 0 | 0 | 0 | 0 | 0 |

*Note.* All the reported values are in anisotropic conditions.

**Table 7**
*Residence Times at Different Probability Values of the Cumulative Frequency Distributions ($T_{90\%}$, $T_{80\%}$, $T_{50\%}$, $T_{20\%}$, and $T_{10\%}$; Days) in Isotropic and Anisotropic and Neutral Conditions*

| Stream flow | Isotropic condition | | | | | | Anisotropic condition | | | | | |
|---|---|---|---|---|---|---|---|---|---|---|---|---|
| | $T_{90\%}$ | $T_{80\%}$ | $T_{50\%}$ | $T_{20\%}$ | $T_{10\%}$ | $T_{\text{mean}}$ | $T_{90\%}$ | $T_{80\%}$ | $T_{50\%}$ | $T_{20\%}$ | $T_{10\%}$ | $T_{\text{mean}}$ |
| $Q_{\text{avg}}$ | 91 | 72.5 | 38 | 13 | 6 | 39.7 | 97.5 | 80 | 37 | 5 | 4 | 53 |
| $Q_{\text{bf}}$ | 94.5 | 80.5 | 48 | 21 | 11 | 50.8 | 99 | 84 | 49.5 | 14 | 10 | 55.5 |

A power law form was assumed for function $f$ () in Equations 3 and 4 which, after log-transformation, takes on the following linear forms:

$$\log F^{neutral} = \log a + b \log Re + c \log \frac{K_v}{K_h} \tag{5}$$

$$\log F^{gain/los} = \log m + n \log Re + g \log \left| \frac{q_{bot}}{v} \right| \tag{6}$$

MLR was performed on the linear forms (Equations 5 and 6) to estimate the regression coefficients ($a$, $b$, $c$, $m$, $n$, and $g$). Multiple model robustness criteria were used for model evaluation; a better model has higher the coefficient of determination ($R^2$), lower Root Mean Square Error ($RMSE$), and lower corrected Akaike information criterion ($AICc$) value, which accounts for the trade-off between model complexity and goodness of fitting (Akaike, 1974).

## 3. Results and Discussion

### 3.1. Hydraulic Head Distribution on the Streambed

2-D spatial water surface elevation maps (Figure 1) are obtained for each $Q_{\text{surf}}$ and bar submergence ratio (Table 3). The flow is subcritical in all cases; the Froude number is lower than 0.9 at any point in the domain. The longitudinal head variation is due to both the stream reach slope and the morphology features. Also, the sequence of pools and riffles that forms the alternate bar induces a lateral variation of the head distribution, where the head is higher on the upstream side of the riffles and dissipates gradually through the riffle lee within the subsequent pool (Figure 1). Furthermore, increasing $Q_{\text{surf}}$ as well as decreasing the bar amplitude undermine the lateral head variations. This behavior is due to less horizontal flow displacements (Tonina & Buffington, 2007), as the hydrostatic pressure is dominant compared to the hydrodynamic effect of morphology pattern as SWE rises (compare pressure head distribution of different $Q_{\text{surf}}$ in Figure 1).

In general, the hydraulic head dissipates through the pool-riffle sequence, as it is higher at the upstream side of the riffle and decreases while reaching its lee side. At lower $Q_{\text{surf}}$, a considerable head variation is evident in the longitudinal and transverse directions because the bed topography has more influence on the streamflow at lower submergence ratios. The instability zones (hydraulic jumps and surface waves) are assumed to be absent in the current analysis because of the very smooth variation in streambed elevation with mild-slope bar ($\Delta_{\text{ab}}/\lambda_{\text{ab}} \approx 0.004$) and the low Froude number within the surface domain.

### 3.2. Hyporheic Flow and Area

The value of the hyporheic flux determines the amount of solutes advected into the HZ, which are necessary to fuel the reactions within this biogeochemically active zone (Bardini et al., 2012).

Similarly to the case of large amplitude in Tonina and Buffington (2011) (partially submerged bar), a decrease in $q_h$ is observed when increasing $Q_{\text{surf}}$ (Table 4 and Figure 2). This is caused by an overall decrease in head gradient, due to lower influence of the morphological feature, at higher $Q_{\text{surf}}$. Despite the increase

**Table 8**
*Maximum Hyporheic Depth at Different Probability Values of the Cumulative Frequency Distributions ($Z_{90\%}$, $Z_{80\%}$, $Z_{50\%}$, $Z_{20\%}$, and $Z_{10\%}$; in Meters) in Different Streamflow Cases, and Different Values of Gaining and Losing Conditions ($q_{bot}$ is Expressed as a Fraction of the Hyporheic Exchange Flux in the Neutral Conditions, $q_{hn}$)*

| | $0.5Q_{avg}$ | | | | | | $Q_{avg}$ | | | | | | $2Q_{avg}$ | | | | | | $3Q_{avg}$ | | | | | | $Q_{bf}$ | | | | | |
|---|---|---|---|---|---|---|---|---|---|---|---|---|---|---|---|---|---|---|---|---|---|---|---|---|---|---|---|---|---|---|
| | $Z_{90\%}$ | $Z_{80\%}$ | $Z_{50\%}$ | $Z_{20\%}$ | $Z_{10\%}$ | $Z_{mean}$ | $Z_{90\%}$ | $Z_{80\%}$ | $Z_{50\%}$ | $Z_{20\%}$ | $Z_{10\%}$ | $Z_{mean}$ | $Z_{90\%}$ | $Z_{80\%}$ | $Z_{50\%}$ | $Z_{20\%}$ | $Z_{10\%}$ | $Z_{mean}$ | $Z_{90\%}$ | $Z_{80\%}$ | $Z_{50\%}$ | $Z_{20\%}$ | $Z_{10\%}$ | $Z_{mean}$ | $Z_{90\%}$ | $Z_{80\%}$ | $Z_{50\%}$ | $Z_{20\%}$ | $Z_{10\%}$ | $Z_{mean}$ |
| $q_{bot} = 0$ (neutral) | 8.38 | 6.45 | 2.43 | 0.63 | 0.42 | 4.59 | 7.82 | 5.87 | 2.01 | 0.62 | 0.42 | 3.73 | 6.49 | 4.78 | 1.53 | 0.57 | 0.4 | 2.76 | 5.16 | 3.76 | 1.15 | 0.54 | 0.38 | 2.09 | 4.79 | 3.84 | 1.83 | 0.60 | 0.43 | 2.03 |
| $q_{bot} = +0.5q_{hn}$ | | | | | | | 4.31 | 3.09 | 1.25 | 0.77 | 0.62 | 1.93 | | | | | | | | | | | | | 2.69 | 2.05 | 0.79 | 0.28 | 0.2 | 1.06 |
| $q_{bot} = -0.5q_{hn}$ | | | | | | | 3.28 | 2.16 | 1.00 | 0.67 | 0.57 | 1.78 | | | | | | | | | | | | | 2.75 | 2.15 | 0.92 | 0.32 | 0.23 | 1.12 |
| $q_{bot} = +q_{hn}$ | 1.25 | 0.92 | 0.55 | 0.30 | 0.23 | 0.6 | 2.32 | 1.39 | 0.68 | 0.36 | 0.29 | 0.9 | 2.18 | 0.96 | 0.65 | 0.38 | 0.3 | 0.9 | 1.3 | 0.96 | 0.65 | 0.38 | 0.3 | 0.69 | 1.28 | 0.96 | 0.38 | 0.22 | 0.17 | 0.55 |
| $q_{bot} = -q_{hn}$ | 1.43 | 1.02 | 0.62 | 0.37 | 0.3 | 0.88 | 1.71 | 1.01 | 0.62 | 0.38 | 0.3 | 0.91 | 2.09 | 1.34 | 0.65 | 0.39 | 0.32 | 0.86 | 1.57 | 1.05 | 0.67 | 0.37 | 0.29 | 0.73 | 1.41 | 1.14 | 0.46 | 0.27 | 0.21 | 0.64 |
| $q_{bot} = +1.5q_{hn}$ | | | | | | | 1.03 | 0.86 | 0.56 | 0.32 | 0.26 | 0.55 | | | | | | | | | | | | | 0.46 | 0.37 | 0.27 | 0.18 | 0.15 | 0.29 |
| $q_{bot} = -1.5q_{hn}$ | | | | | | | 1.41 | 1.06 | 0.58 | 0.35 | 0.29 | 0.59 | | | | | | | | | | | | | 0.56 | 0.38 | 0.26 | 0.19 | 0.17 | 0.33 |
| $q_{bot} = +2q_{hn}$ | 0.72 | 0.58 | 0.25 | 0.06 | 0.03 | 0.33 | 1 | 0.83 | 0.48 | 0.28 | 0.1 | 0.46 | 0.89 | 0.74 | 0.42 | 0.18 | 0.1 | 0.41 | 0.71 | 0.62 | 0.44 | 0.30 | 0.26 | 0.4 | 0.37 | 0.31 | 0.23 | 0.17 | 0.15 | 0.25 |
| $q_{bot} = -2q_{hn}$ | 1.06 | 0.73 | 0.41 | 0.28 | 0.25 | 0.41 | 1.24 | 0.56 | 0.40 | 0.30 | 0.28 | 0.46 | 0.85 | 0.73 | 0.50 | 0.35 | 0.3 | 0.48 | 0.77 | 0.65 | 0.46 | 0.28 | 0.2 | 0.44 | 0.57 | 0.48 | 0.32 | 0.22 | 0.18 | 0.36 |
| $q_{bot} = +3q_{hn}$ | 0 | 0 | 0 | 0 | 0 | 0 | 0.75 | 0.60 | 0.30 | 0.11 | 0.08 | 0.38 | 0.88 | 0.68 | 0.29 | 0.10 | 0.07 | 0.36 | 0.63 | 0.56 | 0.38 | 0.26 | 0.11 | 0.34 | 0 | 0 | 0 | 0 | 0 | 0 |
| $q_{bot} = -3q_{hn}$ | 0 | 0 | 0 | 0 | 0 | 0 | 1.11 | 0.64 | 0.40 | 0.28 | 0.24 | 0.43 | 0.67 | 0.56 | 0.40 | 0.30 | 0.27 | 0.39 | 0.65 | 0.59 | 0.36 | 0.21 | 0.1 | 0.35 | 0 | 0 | 0 | 0 | 0 | 0 |

*Note.* All the reported values are in anisotropic conditions.

**Table 9**
*Maximum Hyporheic Depth at Different Probability Values of the Cumulative Frequency Distributions ($Z_{90\%}$, $Z_{80\%}$, $Z_{50\%}$, $Z_{20\%}$, and $Z_{10\%}$; in Meters) in Isotropic and Anisotropic and Neutral Conditions*

| Stream flow | Isotropic condition | | | | | | Anisotropic condition | | | | | |
|---|---|---|---|---|---|---|---|---|---|---|---|---|
| | $Z_{90\%}$ | $Z_{80\%}$ | $Z_{50\%}$ | $Z_{20\%}$ | $Z_{10\%}$ | $Z_{mean}$ | $Z_{90\%}$ | $Z_{80\%}$ | $Z_{50\%}$ | $Z_{20\%}$ | $Z_{10\%}$ | $Z_{mean}$ |
| $Q_{avg}$ | 35.74 | 29.49 | 15.59 | 4.43 | 1.03 | 14.09 | 7.82 | 5.87 | 2.01 | 0.62 | 0.42 | 3.73 |
| $Q_{bf}$ | 27.87 | 22.82 | 11.73 | 3.54 | 1.25 | 11.14 | 4.79 | 3.84 | 1.83 | 0.6 | 0.43 | 2.03 |

in $A_h$, as a larger portion of the alternate bar is submerged (Table 3), $Q_h$ plummets because of the significant decrease in $q_h$ (Table 4 and Figure 2).

Besides the hydraulic head gradients along the streambed, the hyporheic flow field is also influenced by vertical head gradients that are induced by $q_{bot}$. In agreement with Trauth et al. (2013), the imposed gaining

**Table 10**
*Regression Coefficients for Equation 7 (Neutral Condition).*

| $F^{neutral}$ | Regression coefficients | | | | | | | | | $R^2$ | AIC | RMSE |
|---|---|---|---|---|---|---|---|---|---|---|---|---|
| | $a$ | $SE_a$ | $P.Val_a$ | $b$ | $SE_b$ | $P.Val_b$ | $c$ | $SE_c$ | $P.Val_c$ | | | |
| $\dfrac{q_h}{v}$ | 1.71 | 0.69 | 0.07 | −1.25 | 0.11 | $4E-4$ | 0.71 | 0.06 | $3E-4$ | 0.99 | −7.12 | 0.071 |
| $\dfrac{Q_h}{Q_{surf}}$ | 7.42 | 1.08 | 0.002 | −1.85 | 0.18 | $5E-4$ | 0.64 | 0.09 | 0.002 | 0.98 | −0.95 | 0.11 |
| $\dfrac{T_{90\%}K_v}{d}$ | 1.7 | 0.08 | $3E-5$ | −0.45 | 0.01 | $4.7E-6$ | 0.98 | 0.007 | $1.5E-8$ | 0.93 | −37.1 | 0.08 |
| $\dfrac{T_{80\%}K_v}{d}$ | 1.52 | 0.17 | $8E-4$ | −0.43 | 0.03 | $9E-5$ | 0.98 | 0.01 | $3E-7$ | 0.999 | −27.1 | 0.02 |
| $\dfrac{T_{50\%}K_v}{d}$ | 1.05 | 0.91 | 0.31 | −0.4 | 0.15 | 0.06 | 1.07 | 0.08 | $2E-4$ | 0.98 | −3.3 | 0.09 |
| $\dfrac{T_{20\%}K_v}{d}$ | −3.06 | 0.6 | 0.007 | 0.21 | 0.1 | 0.09 | 1.31 | 0.05 | $1E-5$ | 0.99 | −9.2 | 0.06 |
| $\dfrac{T_{10\%}K_v}{d}$ | −3.69 | 0.6 | 0.004 | 0.27 | 0.1 | 0.05 | 1.15 | 0.05 | $2E-5$ | 0.99 | −9.1 | 0.06 |
| $\dfrac{T_{mean}K_v}{d}$ | 1.17 | 0.6 | 0.12 | −0.41 | 0.1 | 0.02 | 0.93 | 0.05 | $6E-5$ | 0.99 | −9.1 | 0.06 |
| $\dfrac{z_{90\%}}{d}$ | 6.3 | 0.38 | $7E-5$ | −0.8 | 0.06 | $2E-4$ | 0.7 | 0.03 | $3E-5$ | 0.99 | −15.6 | 0.04 |
| $\dfrac{z_{80\%}}{d}$ | 6.3 | 0.3 | $3E-5$ | −0.8 | 0.05 | $8E-5$ | 0.74 | 0.03 | $8E-6$ | 0.99 | −19.06 | 0.03 |
| $\dfrac{z_{50\%}}{d}$ | 5.9 | 0.72 | 0.001 | −0.8 | 0.12 | 0.003 | 0.9 | 0.06 | $1E-4$ | 0.98 | −6.63 | 0.04 |
| $\dfrac{z_{20\%}}{d}$ | 4.03 | 0.29 | $2E-4$ | −0.56 | 0.05 | $3E-4$ | 0.83 | 0.02 | $5E-6$ | 0.997 | −19.5 | 0.03 |
| $\dfrac{z_{10\%}}{d}$ | 2.68 | 0.33 | 0.001 | −0.43 | 0.05 | 0.001 | 0.44 | 0.03 | $9E-5$ | 0.99 | −17.7 | 0.03 |
| $\dfrac{z_{mean}}{d}$ | 6.77 | 0.5 | $1E-4$ | −0.93 | 0.08 | $3E-4$ | 0.65 | 0.04 | $1E-4$ | 0.99 | −11.8 | 0.05 |

*Note:* p.Val and SE are the p-value and standard error associated with each coefficient, respectively.

**Table 11**
*Regression Coefficients for Equation 8 (Gaining/Losing Conditions)*

| $F^{\text{gain/los}}$ | Regression coefficients | | | | | | | | | $R^2$ | $AIC$ | $RMSE$ |
| | $a$ | $SE_a$ | $P.Val_a$ | $b$ | $SE_b$ | $P.Val_b$ | $c$ | $SE_c$ | $P.Val_c$ | | | |
|---|---|---|---|---|---|---|---|---|---|---|---|---|
| $\dfrac{q_h}{v}$ | 0.81 | 0.8 | 0.31 | $-1.02$ | 0.19 | $7E-7$ | 0.21 | 0.11 | 0.07 | 0.77 | $-19.7$ | 0.11 |
| $\dfrac{Q_h}{Q_{surf}}$ | 6.02 | 1.443 | $2E-4$ | $-3.16$ | 0.34 | $1.8E-10$ | $-1.22$ | 0.2 | $8E-7$ | 0.74 | 20.4 | 0.31 |
| $\dfrac{T_{90\%}K_v}{d}$ | $-0.59$ | 0.38 | 0.13 | $-1.22$ | 0.09 | $1E-14$ | $-0.84$ | 0.05 | $2E-16$ | 0.9 | $-70.4$ | 0.08 |
| $\dfrac{T_{80\%}K_v}{d}$ | $-1.48$ | 0.44 | 0.002 | $-1.06$ | 0.11 | $2E-11$ | $-0.81$ | 0.06 | $3E-14$ | 0.85 | $-59.8$ | 0.1 |
| $\dfrac{T_{50\%}K_v}{d}$ | $-3.07$ | 0.45 | $1E-7$ | $-0.62$ | 0.11 | $2E-6$ | $-0.6$ | 0.06 | $1E-10$ | 0.75 | $-59$ | 0.1 |
| $\dfrac{T_{20\%}K_v}{d}$ | $-3.61$ | 0.6 | $2E-7$ | $-0.52$ | 0.13 | $4E-4$ | $-0.53$ | 0.08 | $7E-8$ | 0.63 | $-45.2$ | 0.11 |
| $\dfrac{T_{10\%}K_v}{d}$ | $-3.33$ | 0.73 | $8E-5$ | $-0.66$ | 0.17 | $7E-4$ | $-0.6$ | 0.1 | $2E-6$ | 0.53 | $-25.5$ | 0.16 |
| $\dfrac{T_{mean}K_v}{d}$ | $-1.63$ | 0.38 | $2E-4$ | $-0.7$ | 0.09 | $7E-9$ | $-0.5$ | 0.05 | $8E-11$ | 0.75 | $-70.7$ | 0.08 |
| $\dfrac{z_{90\%}}{d}$ | 5.48 | 0.77 | $6E-8$ | $-1.61$ | 0.18 | $7E-10$ | $-0.68$ | 0.11 | $5E-7$ | 0.71 | $-21.6$ | 0.17 |
| $\dfrac{z_{80\%}}{d}$ | 4.68 | 0.72 | $3E-7$ | $-1.42$ | 0.17 | $2E-9$ | $-0.6$ | 0.1 | $1E-6$ | 0.69 | $-27.8$ | 0.15 |
| $\dfrac{z_{50\%}}{d}$ | 3.9 | 0.64 | $9E-7$ | $-1.15$ | 0.15 | $2E-8$ | $-0.4$ | 0.09 | $4E-5$ | 0.65 | $-34.5$ | 0.14 |
| $\dfrac{z_{20\%}}{d}$ | 3.23 | 0.9 | $1E-3$ | $-1.03$ | 0.21 | $4E-5$ | $-0.38$ | 0.13 | $5E-3$ | 0.43 | $-11.2$ | 0.19 |
| $\dfrac{z_{10\%}}{d}$ | 3.44 | 1.07 | 0.003 | $-1.17$ | 0.25 | $7E-5$ | $-0.46$ | 0.15 | $4E-3$ | 0.41 | 0.28 | 0.23 |
| $\dfrac{z_{mean}}{d}$ | 5.48 | 0.77 | $6E-8$ | $-1.61$ | 0.18 | $7E-10$ | $-0.68$ | 0.11 | $5E-7$ | 0.71 | $-21.6$ | 0.17 |

*Note:* p.Val and SE are the p-value and standard error associated with each coefficient, respectively.

and losing fluxes decrease $Q_h$ values (Figure 3) and significantly shrink $A_h$ in all streamflow cases (Figure 2 for $Q_{\text{avg}}$ and $Q_{\text{bf}}$). Nevertheless, the shrinkage rate is similar between all streamflow cases (Table 4). It is due to either the loss of some flow paths within the subsurface domain or hindering of some surface particles from entering the subsurface domain. In other words, in losing conditions, some particles (flow paths) enter the subsurface domain without coming back again to the surface water due to the relatively strong vertical negative gradient caused by the assigned negative flux on the domain bottom. On the other hand, in gaining conditions, they are hampered from entering the subsurface domain, as the streambed pressure gradient is overcome by the upward vertical gradient that is induced by the upwelling $q_{\text{bot}}$. At very strong $q_{\text{bot}}$, the HZ disappears under the cases of very low streamflow ($0.5Q_{\text{avg}}$) and bankfull streamflow ($Q_{\text{bf}}$) due to the large magnitude of $q_{\text{bot}}$, that is proportional to the value of $q_h$ in neutral conditions, compared to the $q_h$ induced by the head variation of the surface water.

Peculiarly, there are some discrepancies in $Q_h$ values and behavior between losing and gaining conditions. It can be explained by the differences between the spatial extent of infiltrating cells (Figure 9 in Trauth et al., 2013), as different cells are activated in each streamflow case. In partially submerged bars with low
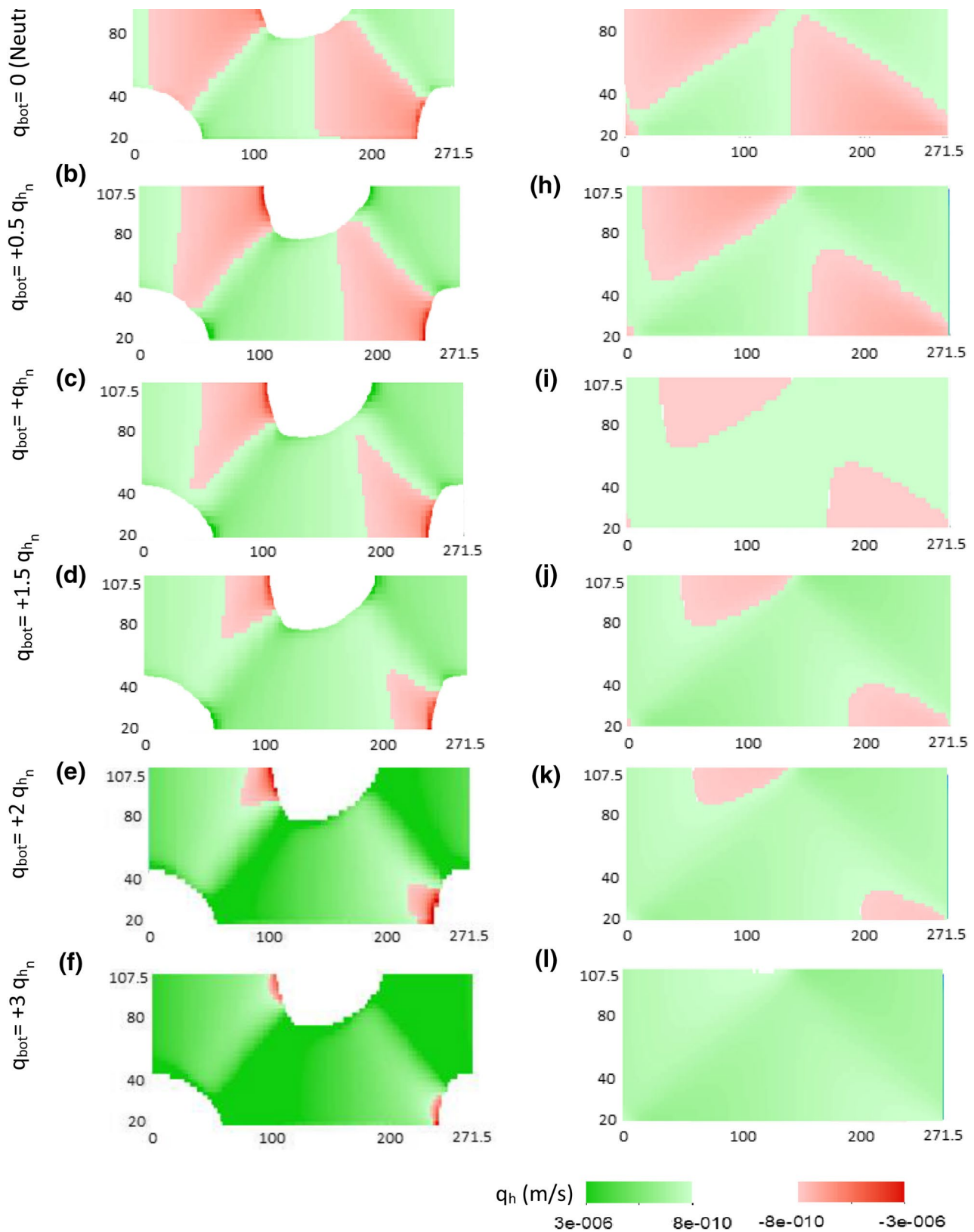
**Figure 2.** Hyporheic flux rate ($q_h$, m/s) spatial distribution over the middle bar in $Q_{avg}$ (left column; a–f) and $Q_{bf}$ (right column; g–l) under different ambient groundwater flux ($q_{bot}$) in anisotropic conditions. The red areas denote downwelling (losing) areas while the green ones indicate the upwelling (gaining) zones. The numbers in each panel that are written on the horizontal and vertical axes represent the streamwise and spanwise coordinates (in meters), respectively.
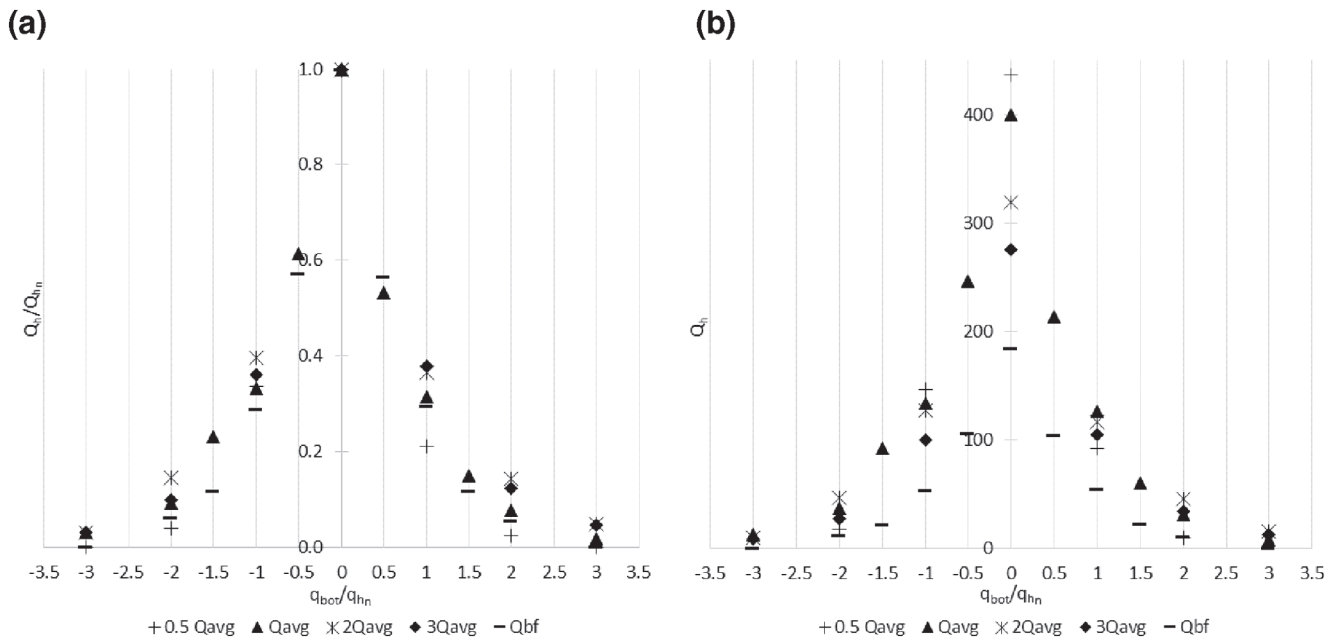
**(a)**

**(b)**

**Figure 3.** (a) Normalized hyporheic exchange flow ($Q_h$ / $Q_{h_n}$) and (b) absolute hyporheic exchange flow ($q_h$) values, in the anisotropic conditions. $q_{bot}$ / $q_{h_n}$ on the horizontal axes represents gaining (positive sign) and losing (negative sign) conditions, where $q_{bot}$ is the value of imposed ambient groundwater. $Q_{h_n}$ and $q_{h_n}$ are the hyporheic flow and flux, respectively, in the neutral condition.



**(c)**

**(d)**
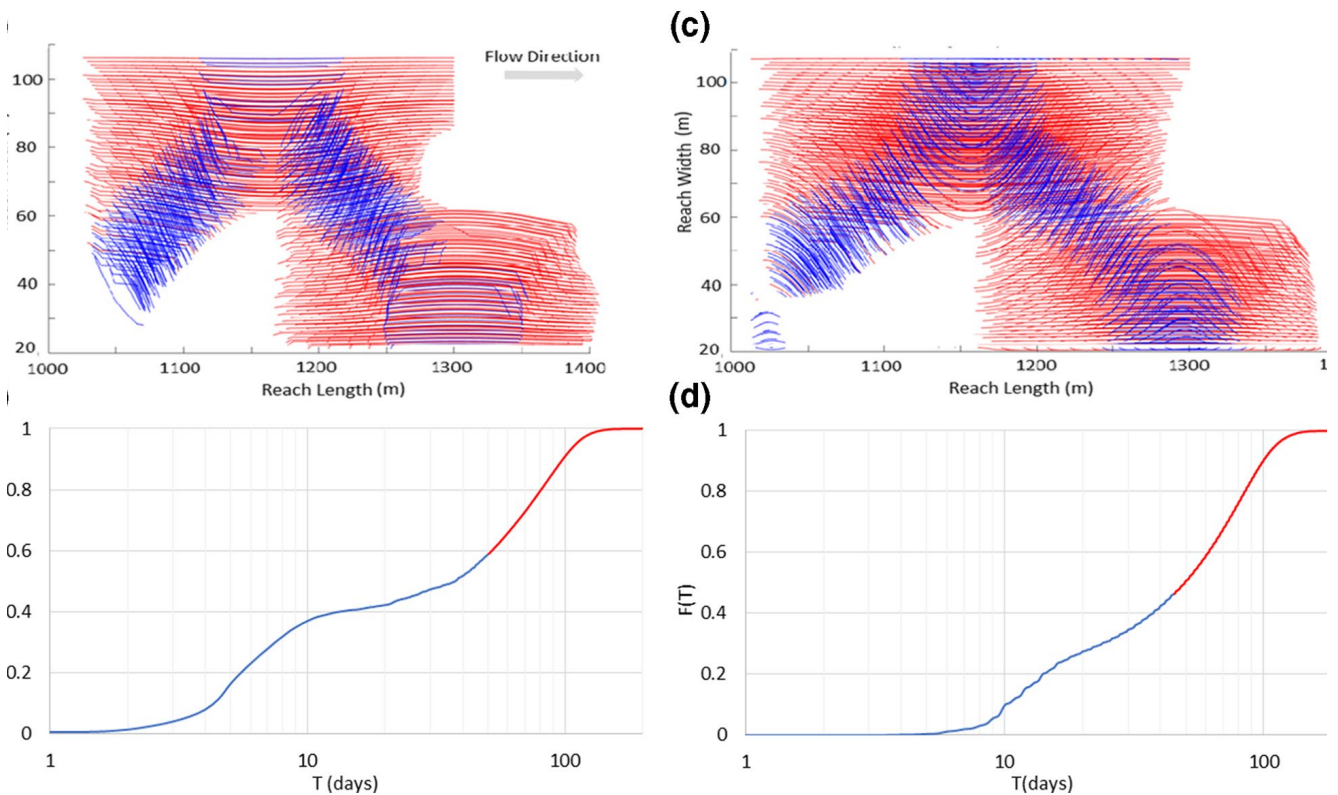
**Figure 4.** Shallow flow paths (blue paths) and deep flow paths (red paths) directions and their associated $T - CD$ under $Q_{avg}$ (a and b), and $Q_{bf}$ (c and d) cases, in neutral and anisotropic conditions. The blue and red parts of the $T - CD$ line correspond to the blue paths and the red paths, respectively.
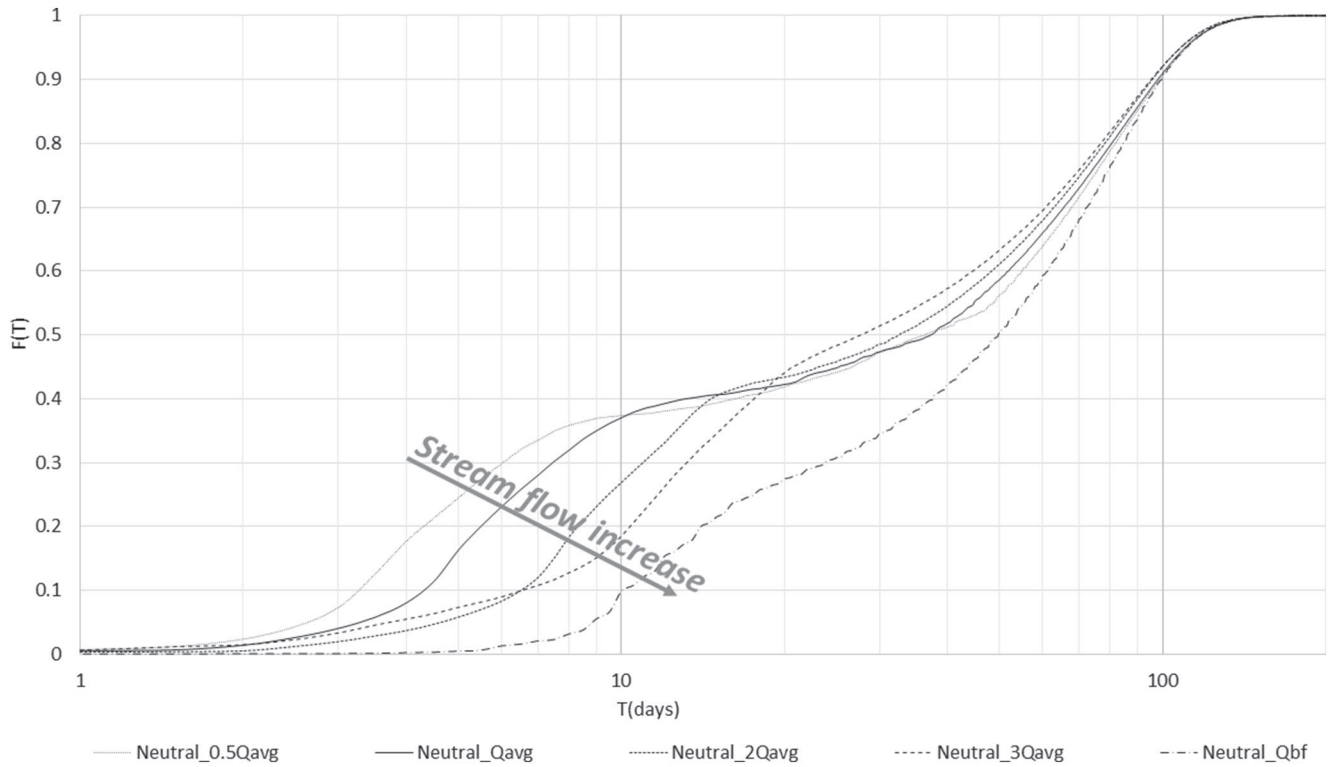
**Figure 5.** Cumulative frequency distribution of residence times (F(T)) in neutral and anisotropic conditions under different streamflow cases ($0.5Q_{avg}$, $Q_{avg}$, $2Q_{avg}$, $3Q_{avg}$, and $Q_{bf}$). The gray arrow represents the direction of increasing the streamflow value.
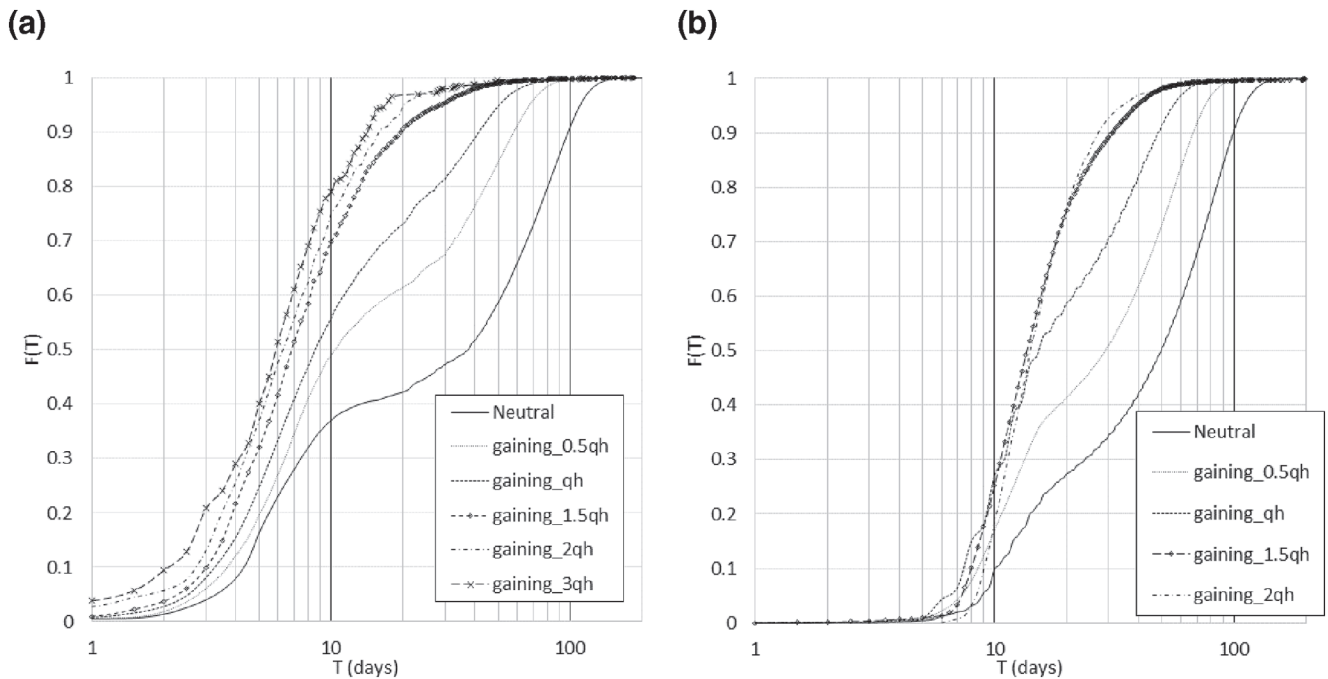


**Figure 6.** Cumulative frequency distribution of residence times (F(T)) under different gaining fluxes ($q_{bot} = 0, +0.5q_{h_n}, +q_{h_n}, +1.5q_{h_n}, +2q_{h_n}$ and $+3q_{h_n}$), and different $Q_{surf}$ cases ([a] $Q_{avg}$ and [b] $Q_{bf}$), in anisotropic conditions.
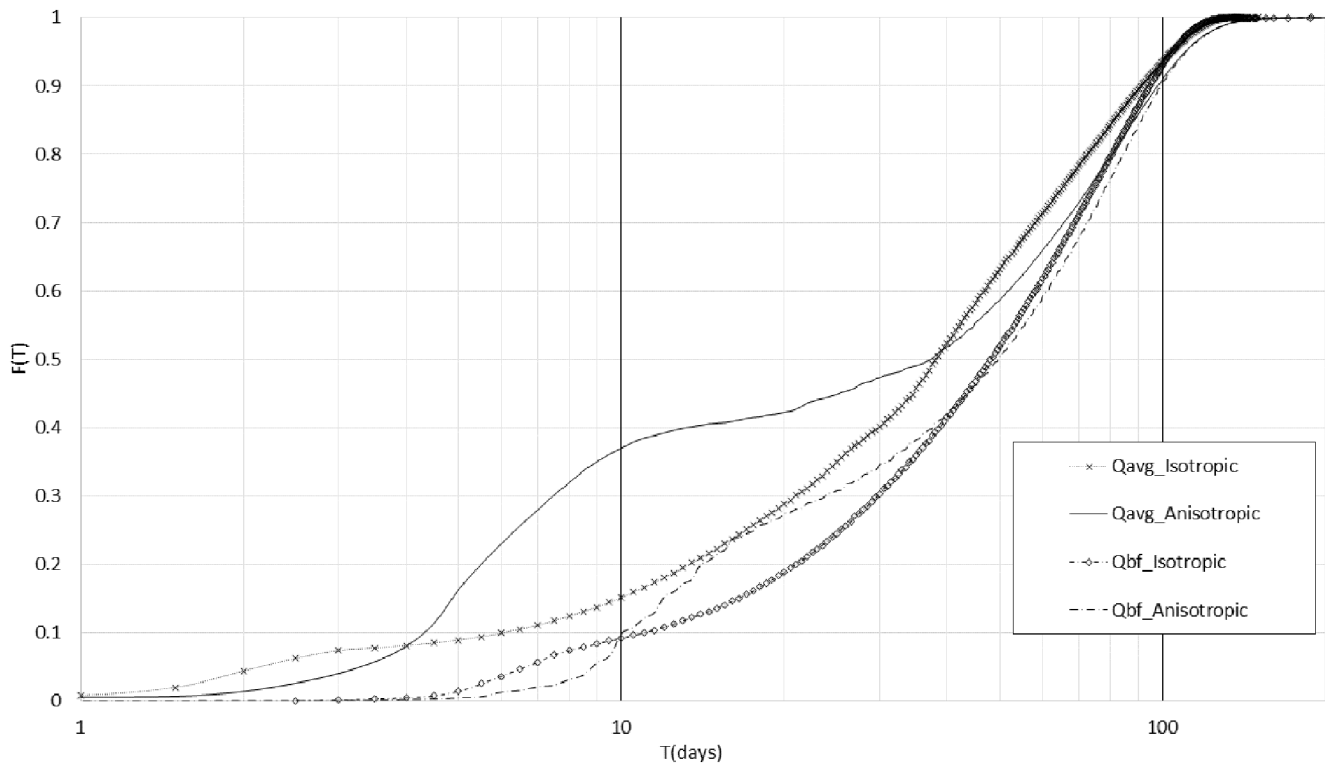
**Figure 7.** Cumulative frequency distribution of residence times (F(T)) in isotropic and anisotropic conditions, for $Q_{avg}$ and $Q_{bf}$ in neutral conditions.

$Q_{surf}$ ($0.5Q_{avg}$, $Q_{avg}$, and $2Q_{avg}$), $Q_h$ is more hampered by $q_{bot}$ in gaining condition than in the losing one. Contrarily, and in agreement with fully submerged bars in Trauth et al. (2013), for $3Q_{avg}$ and $Q_{bf}$, in general, $Q_h$ is slightly higher in gaining than in losing conditions. One possible explanation of this behavior is discussed by Tonina and Buffington (2007), who stated that the strength of the pressure gradient is not always decreasing with higher submergence. Instead, at a certain point, it can increase again, which implies a change in the hyporheic exchange mechanism. Also, In partially submerged bars, the existence of dry cells around the bars peaks could contribute to these discrepancies, unlike the case of fully submerged bars.

The sediment properties, especially hydraulic conductivity, are key parameters in determining the HZ characteristics. In gravel sediments, $q_h$ is strongly affected by the vertical hydraulic conductivity (Glose et al., 2019). In other words, increasing the vertical conductivity from $10^{-4}$ to $10^{-3}$ m/s in the isotropic conditions decreases the sediment resistance to the flow paths penetration into the streambed. Therefore, $q_h$ increases by almost the same order of magnitude as $K_z$, while $A_h$ is slightly lower. This decrease in $A_h$ could not compensate the increase in $q_h$, thus resulting in higher values of $Q_h$ in isotropic conditions (Table 5).

### 3.3. Hyporheic Residence Times

The longitudinal and lateral flow paths within the HZ can be divided into shallow and deep flow paths (Figure 4). These two groups create a bimodal cumulative distribution of $T$, which is demonstrated by the double-S shape of the $T - CD$ (Figures 4b and 4d). The bimodality was verified by applying HDSw/BC(Irr) (Kang & Noh, 2019) and HDS (Hartigan et al., 1985) tests, as they are very accurate in determining the existence of multimodality (Freeman & Dale, 2013; Kang & Noh, 2019).

First, a group of flow paths travels deeper under the bars as the particles flow into the upstream face of the alternate bar and move longitudinally for a distance of similar magnitude to the bar wavelength $\lambda_{ab}$ to exfiltrate at the downstream bar face (red lines in Figures 4a and 4c). Second, a group of shallow paths travels quasi-laterally through the pool-riffle sequences (blue lines in Figures 4a and 4c). The former ones are mostly influenced by the longitudinal variations of head distribution between the upstream and downstream of

the riffle peak, and they travel for longer distances and remain in the HZ for a longer time (Figure 5 and $T_{90\%}$ and $T_{80\%}$ in Table 6). On the other hand, the shallower ones tend to travel within the sediment domain for a much shorter time (Figure 5 and $T_{20\%}$ and $T_{10\%}$ Table 6) before returning to the surface water domain.

In neutral conditions ($q_{bot} = 0$), the residence times of the deep flow paths slightly decrease with increasing $Q_{surf}$; however, in case of full submergence, $T_{80\%}$ increases marginally (Table 6). Therefore, the values of $T_{80\%}$ in neutral conditions exhibit a slight sensitivity to $Q_{surf}$ variations, implying a weak correlation between the streamflow and T in the deep HZ. On the other hand, while an increase in bar submergence generally undermines the role of pool-riffle sequence in driving the hyporheic exchange by reducing the pressure gradient on the streambed, the shallow hyporheic flow paths travel for a longer time for higher $Q_{surf}$ (see $T_{10\%}$ and $T_{20\%}$ in Table 6 and also Figure 5). (Trauth et al., 2013) found that the median residence times ($T_{50\%}$) decrease with increasing $Q_{surf}$ in case of fully submerged bars. This trend is also present in current results for partially submerged bars (Table 6, $0.5Q_{avg}$ to $3Q_{avg}$), although with some minor deviations (compare $T_{50\%}$ for $0.5Q_{avg}$ and $Q_{avg}$ in Table 6). The previous results indicate that residence times in deep HZ are marginally affected by $Q_{surf}$ variations, unlike T in the shallow HZ which is more influenced by the surface water domain. In agreement with Tonina and Buffington (2011), the mean residence time ($T_{mean}$) decreases with increasing $Q_{surf}$, except for fully submerged bar, in which longer T within the shallow HZ leads $T_{mean}$ to rise again to a higher value than those of partially submerged one.

Generally, T values lessen with raising $q_{bot}$ magnitude (Table 6 and Figure 6). At strong $q_{bot}$, in both gaining and losing conditions, the $T - CD$ shifts from a bimodal to a unimodal distribution (Figure 6). This shift indicates the disappearance of a significant part of the deep HZ, with the two HZ parts merging into a single shallow HZ.

Differently from previous studies (Marzadri et al., 2010; Tonina & Buffington, 2011; Trauth et al., 2013), T-CDs do not follow a Log-Normal distribution. The $T - CD$ is evidently bimodal in anisotropic conditions. In isotropic conditions, even though the bimodality is very mild (Figure 7), it is still identified by the HDSw/BC and HDS tests. Therefore, sediment anisotropy enhances the differences between the two groups of flow paths. This bimodality existence is coherent with the presence of two groups of flow paths in both conditions, reported by Tonina and Buffington (2007) and Trauth et al. (2013). Besides, sediment anisotropy affects the ratio of flow paths that infiltrates into the deep or the shallow zone. In isotropic conditions, more than 85% of the flow paths reach the deep zone, unlike in anisotropic conditions in which the flow paths are
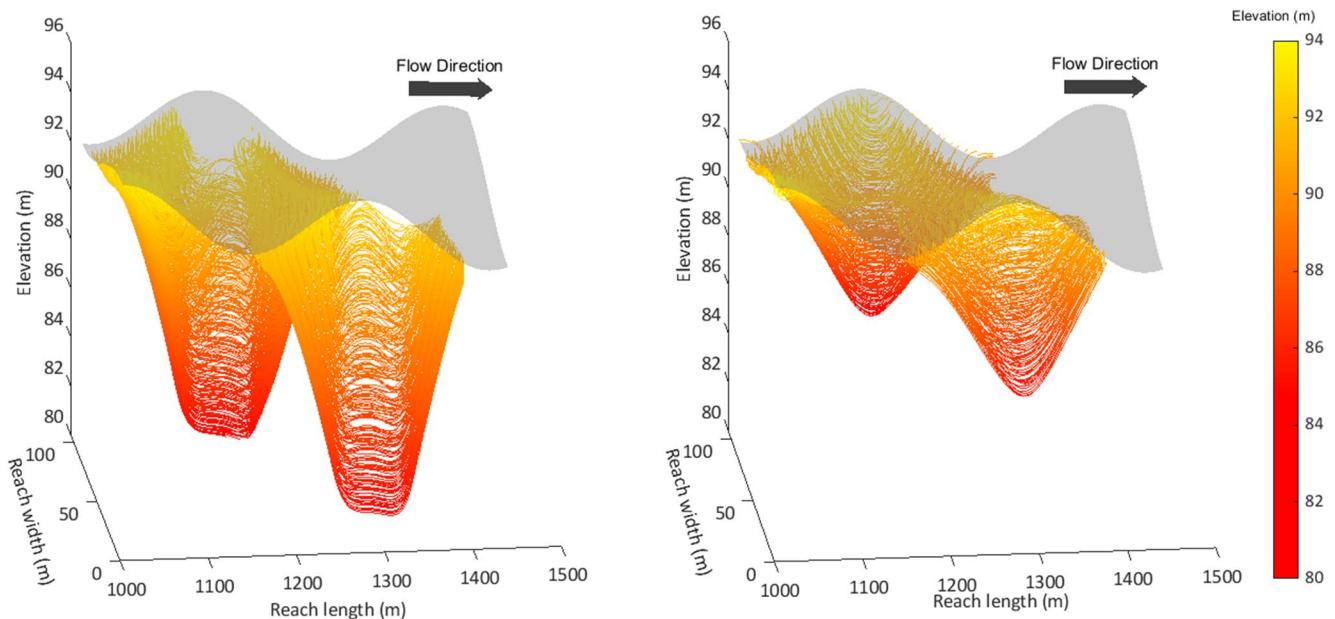


**Figure 8.** Hyporheic flow paths extent, in neutral and anisotropic conditions, within the subsurface domain in (a) $Q_{avg}$ and (b) $Q_{bf}$ cases. The gray surface represents the streambed elevation.
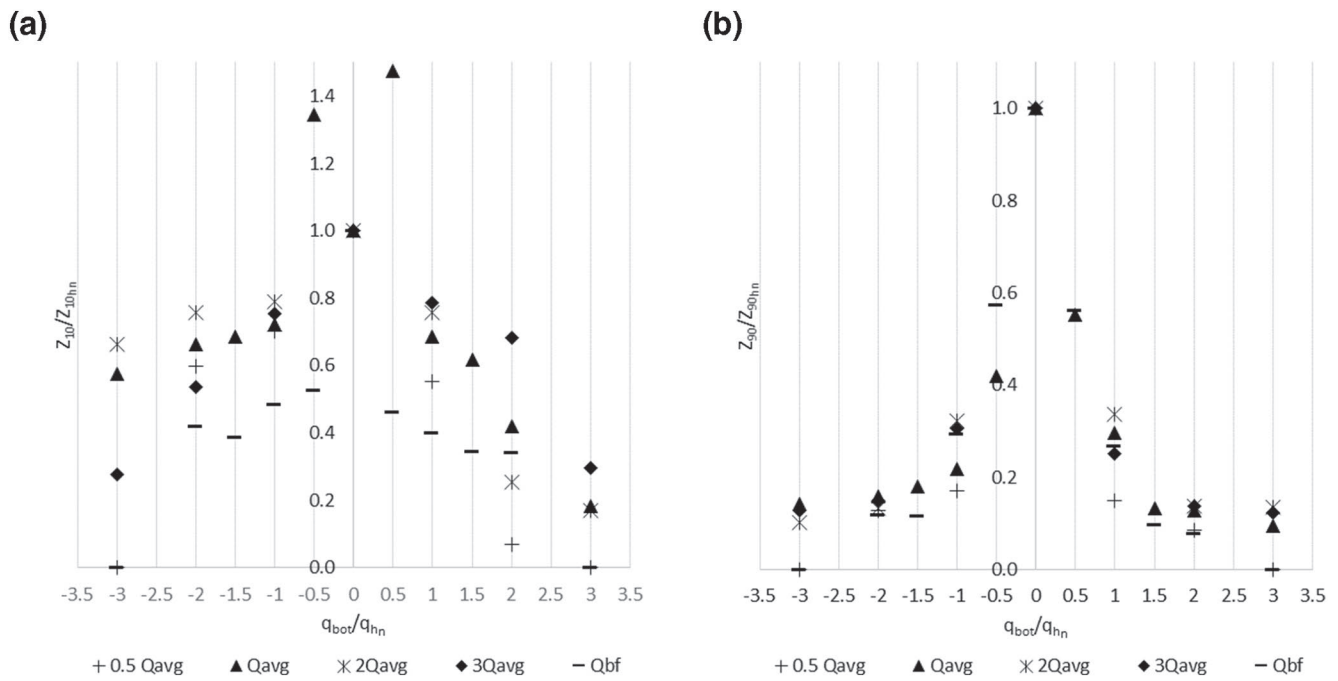
**Figure 9.** (a) Shallow hyporheic depth ($Z_{10}$) normalized by its corresponding value in neutral condition ($Z_{10_{hn}}$). (b) Deep hyporheic depth ($Z_{90}$) normalized by its corresponding value in neutral condition ($Z_{90_{hn}}$). $q_{bot} / q_{h_n}$ on the horizontal axes represents gaining (+ sign) and losing (− sign) conditions, where $q_{bot}$ is the value of imposed ambient groundwater and $q_{h_n}$ is the hyporheic flux in neutral condition. The depths values in both (a and b) refer only to anisotropic conditions.
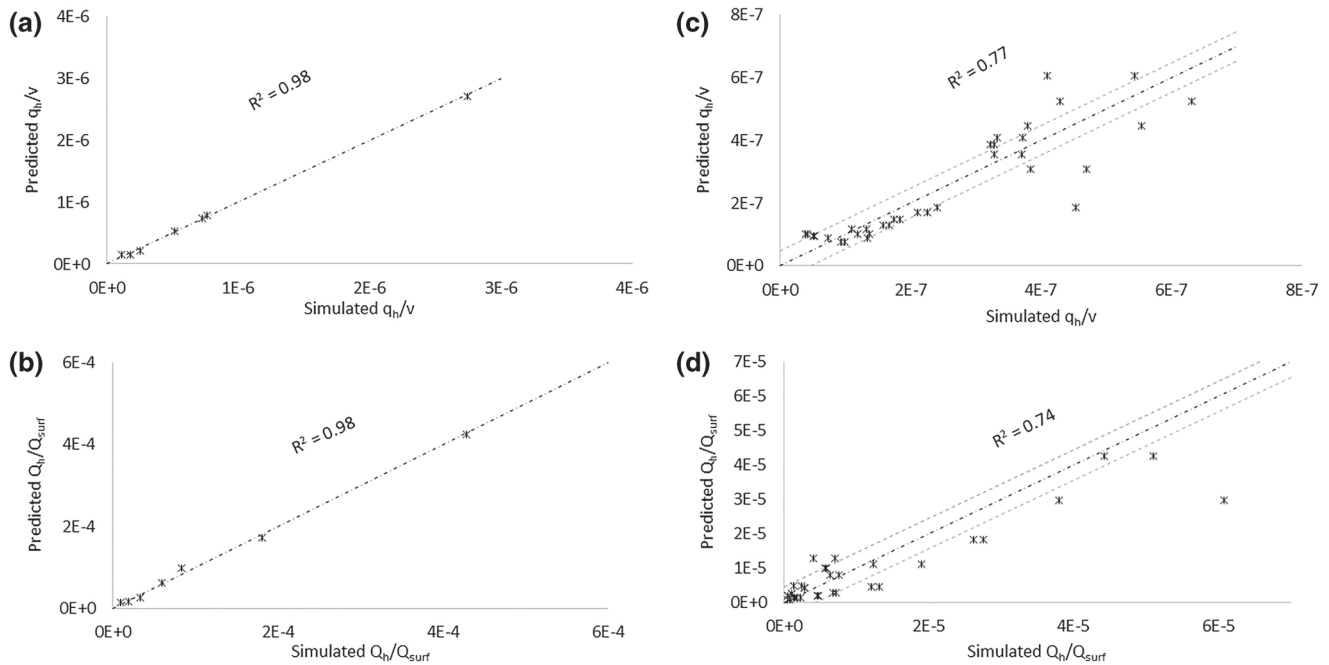


**Figure 10.** Comparison between simulated values of $q_h/v$ and $Q_h/ Q_{surf}$, and the predicted values by Equations 7 and 8; (a and b) are in neutral condition (Equation 7), and (c and d) are in gaining/losing conditions (Equation 8).
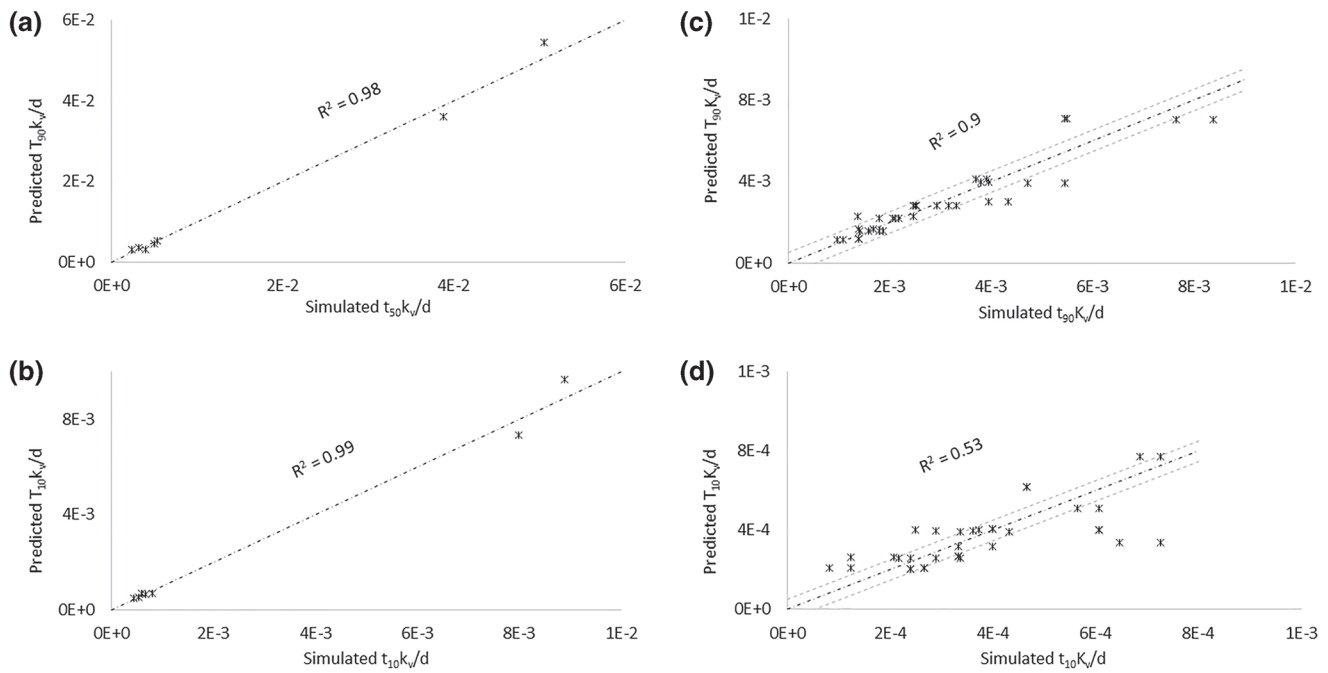
**Figure 11.** Comparison between simulated values of deep and shallow HZ dimensionless residence times ($\frac{T_{90\%K_v}}{d}$ and $\frac{T_{10\%K_v}}{d}$, respectively), and the predicted values by Equations 7 and 8 to the simulations ones; (a and b) are in neutral condition (Equation 7), and (c and d) are in gaining/losing conditions (Equation 8).

almost evenly split between both HZs (Figure 7). In agreement with Marzadri et al. (2010), $T_{mean}$ is slightly longer in anisotropic sediments (Table 7) than in isotropic ones, this is also true for deep flow paths ($T_{90\%}$ and $T_{80\%}$ in Table 7), as the lower vertical resistance to flow allows for faster flow within the sediment. However, shorter residence times ($T_{50\%}$, $T_{20\%}$, and $T_{10\%}$ in Table 7) have smaller values in anisotropic conditions, as the vertical resistance triggers most flow paths to infiltrate in the deep HZ, leaving less portion to form the shallow one.

### 3.4. Hyporheic Depths

The penetration of the flow paths in the HZ delineates the hyporheic depth in the subsurface domain (Figure 8 [for $Q_{avg}$ and $Q_{bf}$]). In the neutral conditions, increasing $Q_{surf}$ decreases the hyporheic depth in both shallow and deep sub-zones for partially submerged bars (Table 8). This decrease in hyporheic depth with increasing $Q_{surf}$ is due to milder pressure head variations on the bars morphology, which is in agreement with the literature results (compare $Z_{mean}$ in Table 8 with Figure 2 in Tonina and Buffington, 2011). This trend does not apply for shallow HZ, which can have a deeper extent in fully submerged bars than in the lower submergence case. This difference can be due to the different portions of flow paths between the shallow and deep HZ.

The imposed gaining and losing conditions decrease the extent of the HZ considerably (Table 8 and Figure 9). The deeper flow paths ($Z_{90\%}$ and $Z_{80\%}$) as well as the mean and median hyporheic depth ($Z_{mean}$, and $Z_{50\%}$, respectively) are more affected by $q_{bot}$ (faster decrease at lower $q_{bot}$) than the depth of the shallow HZ one. This happens because the deep HZ is more interactive with the ambient groundwater (Tables 6 and 8), while the shallow HZ is more linked to surface water. When $q_{bot}$ is higher than $2q_h$, the shallow depths ($Z_{20\%}$ and $Z_{10\%}$ values in Table 8) are also influenced, as the large upwelling flux diminishes the deep HZ extent and interferes with the shallow flow paths.

The lower resistance to the vertical flow in isotropic conditions results in much deeper HZ (Table 9). The increase in the extent of the deep HZ is much higher than for the shallow one, as the latter is more affected by $Q_{surf}$ and the bed morphology.
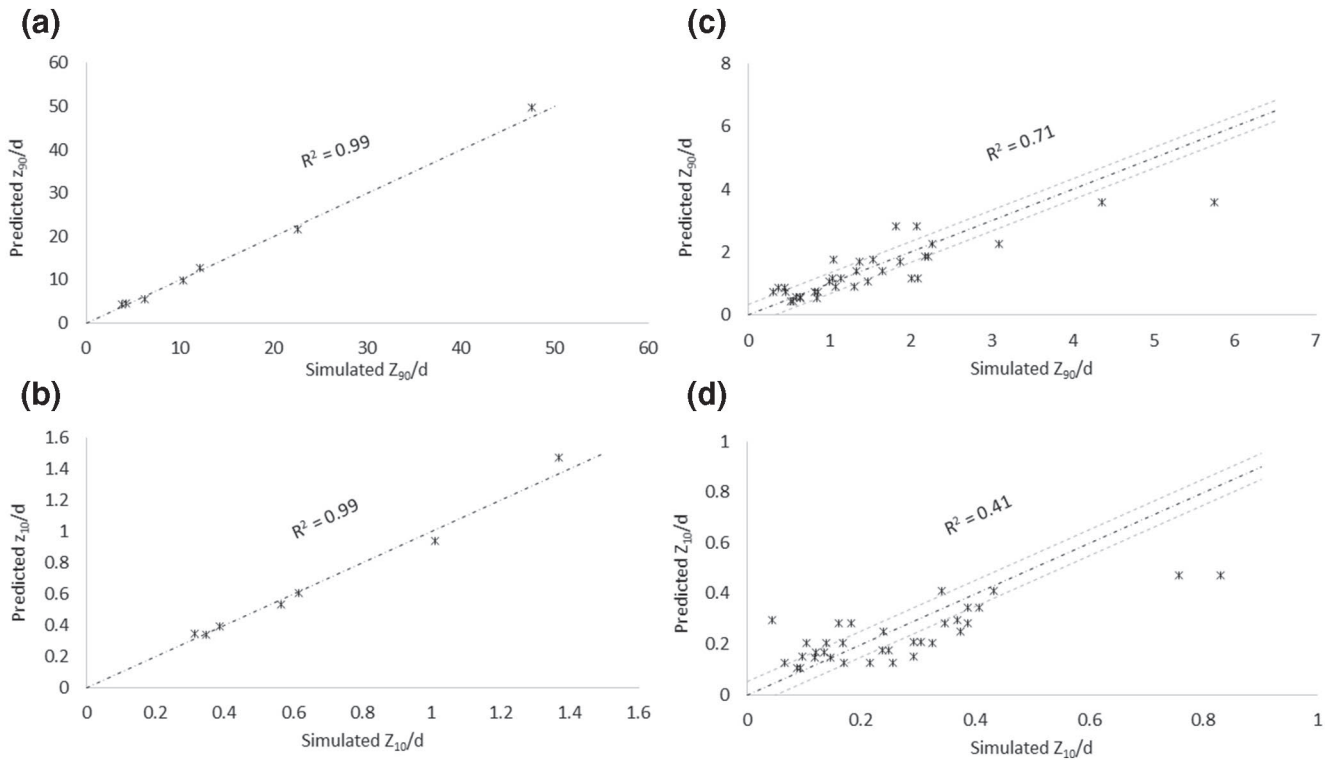
**Figure 12.** Comparison between simulated values of deep and shallow HZ dimensionless hyporheic maximum depths ($\frac{Z_{90\%}}{d}$ and $\frac{Z_{10\%}}{d}$, respectively), and the predicted values by Equations 7 and 8; (a and b) are in neutral condition (Equation 7), and (c and d) are in gaining/losing conditions (Equation 8).

### 3.5. Predictive Model Results

The existing predictive equations proposed in previous studies (Huang & Chui, 2018; Tonina & Buffington, 2011; Trauth et al., 2013) were found to provide erroneous estimate of the results of this study in some conditions (see supporting information). Hence, new equations were developed by performing the MLR to identify coefficient values for Equations 5 and 6.

Both models include all the independent variables, as their variance inflation factor (VIF) did not exceed 5, which indicates no significant correlation exists among the independent variables (no multi-collinearity) (Ott et al., 2004). Consequently, the predictive equations are:

$$F^{neutral} = 10^{(a \pm SE_a)} * Re^{(b \pm SE_b)} * \left(\frac{K_v}{K_h}\right)^{(c \pm SE_c)} \tag{7}$$

$$F^{gain/los} = 10^{(m \pm SE_m)} * Re^{(n \pm SE_n)} * \left|\frac{q_{bot}}{v}\right|^{(g \pm SE_g)} \tag{8}$$

where SE is the standard error associated with the estimated value of each coefficient.

Tables 10 and 11 show the coefficients values, SE and *P*-values of each regression coefficient. In neutral conditions, the model works significantly well in predicting the simulations results ($R^2 > 0.93$) (Figures 10–12 and Table 10). By looking at the regression coefficients values, the Reynolds number has a strong influence on $q_h$ and $Q_h$ values, while $T_{i\%}$ are more affected by sediment anisotropy. Instead, $Z_{i\%}$ are almost equally affected, within error, by both independent variables ($Re$ and $\frac{K_v}{K_h}$).

On the other hand, in gaining and losing conditions, the model predicts reasonably well $q_h$ and $Q_h$ ($R^2 > 0.74$, Figure 10), and it also fits better residence times and hyporheic depths of the deep HZ (most of the predicted values are within 90% confidence interval) than the shallow one (compare $T_{90\%}$ and $Z_{90\%}$ to $T_{10\%}$ and $Z_{10\%}$ in Figures 11 and 12). Similarly to the neutral conditions, $Re$ has a higher effect on $q_h$ and $Q_h$ than the groundwater flux ($\frac{q_{bot}}{v}$) (Table 11).

The novelty of these predictive equations lies in considering the sediment anisotropy as an independent variable. Evidently, it can play a significant role in estimating HZ characteristics, in addition to the inclusion of $q_{bot}$ changes in both gaining and losing conditions. Even though it is hard to build a generalized model, this model helps to understand the dependence of the HZ characteristics on streamflow, sediment anisotropy, and groundwater fluxes.

## 4. Conclusions

The effect of streamflow, thus bar submergence, variations on the HZ characteristics is analyzed in this study. Although the hyporheic exchange area increases with higher submergence, the total hyporheic flow decreases due to the decrease in hyporheic flux per unit streambed area. The HZ is divided into two zones; a shallow zone with quasi-lateral flow paths underneath the pools-riffles sequence, and a deep zone with longitudinal flow paths under the bars peaks. The residence times distribution is bimodal (although this is evident only in anisotropic conditions), which supports the existence of two HZs with different characteristics. The residence times within the shallow zone become longer at a higher bar submergence ratio, while in the deep one, they are less sensitive to streamflow variations. The HZ extent becomes shallower with increasing bar submergence ratio due to less pressure variations on the sediment bed. The presence of ambient groundwater flux reduces the hyporheic exchange flow, residence times, and HZ extent, especially within the deep zone. The HZ characteristics are significantly affected by sediment anisotropy; the hyporheic flow and HZ extent are enhanced considerably in isotropic sediment (higher vertical conductivity) compared to the anisotropic conditions. However, the residence times follow different trends for the shallow and deep zones. A set of the predictive formula was introduced to predict hyporheic flux, residence times, and hyporheic depths and quantify the influence of the three factors discussed in this study (streamflow value, ambient groundwater, and sediment anisotropy). Further investigations need to be carried out with different alternate bars geometry to determine its effect on the HZ characteristics and to expand the predictive model. Finally, the division of the HZs into two zones with different traits is likely to influence the biogeochemical conditions and reactions.

## Data Availability Statement

The data that support the findings of this study are openly available in "HYDROSHARE" at https://doi.org/10.4211/hs.b4f7fbdd9ced4c4e8e5f3b9cbc8843be and cited as Monofy and Boano (2020). Modeling HZ characteristics in alternate bars under different streamflow, ambient groundwater, and sediment anisotropy. HydroShare, http://www.hydroshare.org/resource/b4f7fbdd9ced4c4e8e5f3b9cbc8843be.

## References

Akaike, H. (1974). A new look at the statistical model identification. *IEEE Transactions on Automatic Control*, *19*(6), 716–723.

Bardini, L., Boano, F., Cardenas, M., Revelli, R., & Ridolfi, L. (2012). Nutrient cycling in bedform induced hyporheic zones. *Geochimica et Cosmochimica Acta*, *84*, 47–61. https://doi.org/10.1016/j.gca.2012.01.025

Boano, F., Harvey, J. W., Marion, A., Packman, A. I., Revelli, R., Ridolfi, L., & Wörman, A. (2014). Hyporheic flow and transport processes: Mechanisms, models, and biogeochemical implications. *Reviews of Geophysics*, *52*(4), 603–679.

Da Silva, A. M. F., & Yalin, M. S. (2017). *Fluvial processes*. CRC Press.

Domenico, P. A., & Schwartz, F. W. (1998). Physical and chemical hydrogeology. New York, NY: Wiley.

Freeman, J. B., & Dale, R. (2013). Assessing bimodality to detect the presence of a dual cognitive process. *Behavior Research Methods*, *45*(1), 83–97.

Galloway, J., Fox, A., Lewandowski, J., & Arnon, S. (2019). The effect of unsteady streamflow and stream-groundwater interactions on oxygen consumption in a sandy streambed. *Scientific Reports*, *9*(1), 1–11.

Glose, T. J., Lowry, C. S., & Hausner, M. B. (2019). Vertically integrated hydraulic conductivity: A new parameter for groundwater-surface water analysis. *Groundwater*, *57*(5), 727–736.

Gooseff, M. N. (2010). Defining hyporheic zones–advancing our conceptual and operational definitions of where stream water and groundwater meet. *Geography Compass*, *4*(8), 945–955.

Hartigan, J. A., Hartigan, P. M., et al. (1985). The dip test of unimodality. *Annals of Statistics*, *13*(1), 70–84.

Herzog, S., Higgins, C., & McCray, J. (2016). Engineered streambeds for induced hyporheic flow: Enhanced removal of nutrients, pathogens, and metals from urban streams. *Journal of Environmental Engineering*, *142*(1), 04015053.

Hester, E. T., & Gooseff, M. N. (2010). *Moving beyond the banks: Hyporheic restoration is fundamental to restoring ecological services and functions of streams*. ACS Publications.

Huang, P., & Chui, T. F. M. (2018). Empirical equations to predict the characteristics of hyporheic exchange in a pool-riffle sequence. *Groundwater*, *56*(6), 947–958.

Julien (2002). *River mechanics*. Cambridge University Press.

Kang, Y.-J., & Noh, Y. (2019). Development of Hartigan's dip statistic with bimodality coefficient to assess multimodality of distributions. *Mathematical Problems in Engineering*, *2019*. 1–17. https://doi.org/10.1155/2019/4819475

Keller, E. (1972). Development of alluvial stream channels: A five-stage model. *The Geological Society of America Bulletin*, *83*(5), 1531–1536.

Leopold, L. B., & Wolman, M. G. (1957). *River channel patterns: Braided, meandering, and straight*. US Government Printing Office.

Marzadri, A., Tonina, D., Bellin, A., Vignoli, G., & Tubino, M. (2010). Semianalytical analysis of hyporheic flow induced by alternate bars. *Water Resource Research*, *46*(7). https://doi.org/10.1029/2009wr008285

McDonald, M. G., & Harbaugh, A. W. (1988). A modular three-dimensional finite-difference ground-water flow model. US Geological Survey Reston.

Nelson, P. H., et al. (1994). Permeability-porosity relationships in sedimentary rocks. *The Log Analyst*, *35*(03).

Ott, R. L., Longnecker, M., & Ott, L. (2004). *A first course in statistical methods*. Thomson-Brooks/Cole.

Thibodeaux, L. J., & Boyle, J. D. (1987). Bedform-generated convective transport in bottom sediment. *Nature*, *325*(6102), 341.

Tonina, D., & Buffington, J. M. (2007). Hyporheic exchange in gravel bed rivers with pool-riffle morphology: Laboratory experiments and three-dimensional modeling. *Water Resource Research*, *43*(1).

Tonina, D., & Buffington, J. M. (2009). Hyporheic exchange in mountain rivers i: Mechanics and environmental effects. *Geograpy Compass*, *3*(3), 1063–1086.

Tonina, D., & Buffington, J. M. (2011). Effects of stream discharge, alluvial depth and bar amplitude on hyporheic flow in pool-riffle channels. *Water Resources Research*, *47*(8).

Trauth, N., Schmidt, C., Maier, U., Vieweg, M., & Fleckenstein, J. H. (2013). Coupled 3-d stream flow and hyporheic flow model under varying stream and ambient groundwater flow conditions in a pool-riffle system. *Water Resource Research*, *49*(9), 5834–5850.

USACE (2016). *Hec-ras river analysis system hydraulic reference manual*. Institute of Water Resources, Hydrological Engineering Center Davis.

Van den Berg, J. H. (1995). Prediction of alluvial channel pattern of perennial rivers. *Geomorphology*, *12*(4), 259–279.

Wu, L., Singh, T., Gomez-Velez, J., Nützmann, G., Wörman, A., Krause, S., & Lewandowski, J. (2018). Impact of dynamically changing discharge on hyporheic exchange processes under gaining and losing groundwater conditions. *Water Resources Research*, *54*(12), 10–76.